Results in Engineering 27 (2025) 106781

Contents lists available at ScienceDirect

Results in Engineering

journal homepage: www.sciencedirect.com/journal/results-in-engineering

Research paper

Evaluation of the size and orientation-dependent mechanical properties of additively manufactured Ti-6Al-4V: The role of microstructure, defects, and surface roughness and its implications for lattice structures

M. Casata [a], S. Perosanz [a], Y.T. Tang [b,c], T. Wilkinson [a], R.C. Reed [b], D. Barba [a,*]

[a] E.T.S. de Ingeniería Aeronáutica y del Espacio, Universidad Politécnica de Madrid, Plaza Cardenal Cisneros 3, 28040, Madrid, Spain
[b] Department of Materials Science, University of Oxford, Parks Road, Oxford, OX1 3PH, United Kingdom
[c] School of Metallurgy and Materials, University of Birmingham, Edgbaston, Birmingham, B15 2TT, United Kingdom

ARTICLE INFO

Keywords:
Additive manufacturing
Ti-6Al-4V
Laser powder bed fusion
Size effect
Microstructure
Lattice structures
Mechanical properties

ABSTRACT

Laser powder bed fusion (LPBF) enables the fabrication of complex components beyond conventional methods. However, this complexity introduces variability in the feature size, from large sections to fine struts, leading to differences in thermal and processing history. Even with identical processing conditions and same base alloy, this variability can affect the microstructure, the defects, and the mechanical behaviour of the printed material. This is the case particularly in Ti-6Al-4V, where microstructure depends strongly on thermal history. This work systematically examines the impact of size and LPBF processing conditions on microstructure, defects, and mechanical performance of Ti-6Al-4V. Defect analysis, geometry, and microstructure characterization are conducted to assess the effects of sample size, orientation, and LPBF parameters. Results indicate increased porosity in smaller-sized specimens, while roughness remains largely independent of size. Microstructural analysis reveals α-lath refinement as the size decreases and when high-energy density parameters were used. Then, the mechanical properties of the specimens are extracted accurately based on X-ray tomography and computational modelling. The results show that high roughness causes up to a 5.05% reduction in the load-bearing area of small-size specimens (struts). Once accurately evaluated, the ultimate tensile strength (UTS) and yield strength (YS) are found to increase by 3.87% and 6.65%, respectively, for small-size specimens when compared to large ones, which has been attributed mainly to microstructural changes. The outcomes highlight the significance of size effects and their accurate assessment in the design of LPBF parts.

1. Introduction

Metal Additive Manufacturing (AM) in recent years has evolved from rapid prototyping to a consolidated manufacturing technique that enables the production of components with intricate geometries, revolutionizing fields such as aerospace and biomedical [1–4]. Among all metal AM techniques, laser powder bed fusion (LPBF) is the most widespread in the industry [5]. LPBF is a layer-by-layer process with a laser selectively melting the metal powder bed according to the nominal geometry of the component [6]. LPBF is capable of fabricating components with high geometrical complexity that were previously impossible to create with traditional manufacturing methods. This has enabled new design techniques for lightweighting, such as lattice structures [7]. These structures comprise a network of repeating open-cells in the 3D space with a designed porosity [7,8]. The characteristic size of the printed material varies abruptly in LPBF components [9,10], from sub-mm size for the case of cellular struts to tens of mm for bulk components. This extensive range of characteristic lengths is known to produce a change in the thermal history experienced by the material during manufacturing, affecting the microstructural features [11,12]. This is especially the case for Ti-6Al-4V, which presents a strong dependence of the microstructure on the thermal history of the alloy. This effect, despite being beneficial in conventional manufacturing, providing the versatility of properties observed in Ti-6Al-4V, in the case of LPBF, produces a strong size dependency on the mechanical properties arising from changes in the microstructure and defects produced by the different thermal history. This set an important issue when designing an LPBF component, as heterogeneous sample sizes usually coexist within

* Corresponding author.
E-mail address: daniel.barba@upm.es (D. Barba).

https://doi.org/10.1016/j.rineng.2025.106781
Received 29 April 2025; Received in revised form 5 August 2025; Accepted 15 August 2025

Available online 25 August 2025

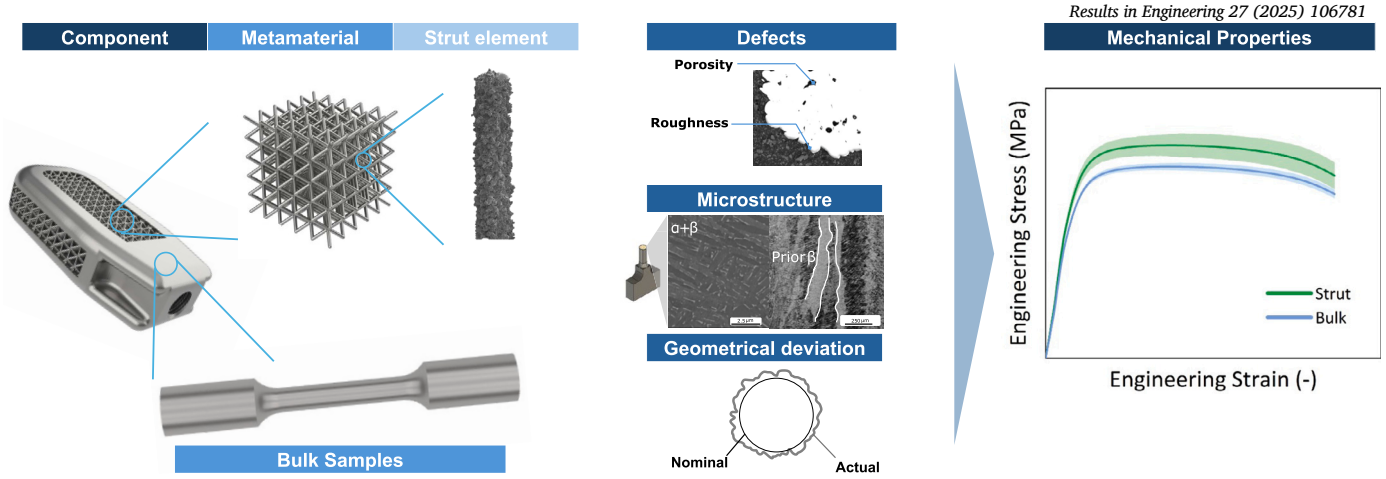

Fig. 1. Overview of the multiscale nature of intrinsic defects, microstructure, and schematic (representative) mechanical properties in AM strut lattice structures.

the same part, as shown in Fig. 1, leading to a heterogeneous range of microstructures, defects, and mechanical properties. Therefore, understanding this material variability and its impact on the properties is of critical importance for the design and development of LPBF Ti-6Al-4V components. This presents a scientific challenge that requires the combination of miniaturized testing, advanced material characterisation, and computational modelling to capture and understand the mechanical properties of the foundational elements, such as struts, in LPBF Ti-6Al-4V cellular metamaterials. This is paramount as the microstructure, defects, and properties manufactured via LPBF change with numerous variables such as processing parameters, sample dimensions, and printing orientation. This has been the focus of multiple previous studies [13–17]. Barba et al. [13] studied the difference in mechanical properties of Ti-6Al-4V samples with a thickness ranging from 0.25 mm to 3 mm. They found that ultimate tensile strength (UTS) and yield stress (YS) decreased as size increased, while ductility increased with the latter. These changes were attributed to the thinner α laths in the microstructure, the higher oxygen enrichment, and higher surface-to-volume ratio impacting struts samples compared to their larger counterpart. Zhang et al. [14] obtained similar results when studying the microstructure of 1.3 and 2 mm diameter Ti-6Al-4V samples and reported their quasi-static and fatigue properties, finding that a 50% roughness decrease in larger samples significantly increased the fatigue life. The impact of the build orientations of elemental struts has also been investigated, showing that an increase in roughness and eccentricity is detrimental to tensile strength [15], ductility [16], and fatigue life [17]. These studies highlight the importance of studying the mechanical properties of the direct in-service geometry of the part to preserve its characteristic microstructural and surface roughness features. In fact, unlike many other manufacturing techniques, limited post-processing is possible in lattice structures due to their intricate geometry. This set some limits for the dimensional accuracy compared to the nominal geometry and for the surface roughness, leading to errors in the estimation of mechanical properties.

So it is clear that additive manufacturing is creating a necessity for developing adapted procedures for the accurate assessment of the material and mechanical properties of small size specimens. The growing focus on small-scale samples emphasizes the importance of developing precise and reliable methods for their characterization and testing, addressing the particularities of strut testing as shown by Rouse et al. [18]. Dzugan et al. [19] studied Ti-6Al-4V mechanical properties of samples produced by LPBF and selective electron beam melting (SEMB) by means of micro tensile testing (MTT) samples. Their results show that surface roughness and porosity influence the calculations of the load-bearing area. They stated that the dimensions calculated via micrometer do not provide accurate results, as they overestimate the cross-sectional area. Therefore, to mitigate this error, they proposed an adjusted load-bearing area using fractography samples to determine and exclude the surface layer. A similar adjustment approach was proposed by June et al. [20] to measure the "true" load-bearing area of thin tensile samples, using the maximum peak height extracted from the surface topography acquired by optical microscopy to correct the caliper measurements. Their results show that this approach leads to comparable results with the ones obtained using the area calculated using X-ray computed tomography (CT) data, which, due to its ability to measure the cross-sectional area along the entire gauge length, and its non-destructive nature, allowing the same specimen to be used for both area measurement and mechanical testing, has been demonstrated to provide accurate and reliable results [21,14]. However, the extensive use of CT is limited due to the inherent costs and time demands associated with this technique. For these reasons, there is a pressing need to understand the difference in intrinsic properties, microstructures, and defects in the samples printed with miniaturized dimensions (similar to the ones found in elementals of lattice structures) from the ones printed with conventional sizes for mechanical testing (with therefore different thermal history and microstructure). Once this is established, it is necessary to develop an accurate and affordable characterization approach to assess the precise calculation of the printed material's mechanical properties and eventually be suitable for integration at the design stage of cellular metamaterials.

With this aim, this study focuses on the systematic study of the effect of size on the microstructure, defects, and mechanical properties between bulk LPBF Ti-6Al-4V samples and struts of miniaturized dimensions (1.5 mm diameter). To do so, two different representative sizes are manufactured, representing bulk and strut elements, and two different LPBF parameter sets are used to analyze the effect of size under various processing conditions. Furthermore, the impact of orientation is addressed in the strut elements by studying four different orientations. A combination of optical microscopy, scanning electron microscopy, and CT-scan analysis is used to study the differences in defects (pores, roughness, geometrical deviation) and microstructure (α laths and prior β grain size). Once the material characterization is addressed, the effect of sample size and orientation on the mechanical behaviour is investigated through mechanical tensile testing. The experimental results are then combined with computational simulation using the CT-scan geometries to accurately address the intrinsic mechanical properties of LPBF Ti-6Al-4V and its dependence on the sample size. Finally, some key points are included to emphasize the implications of the results on the design of LPBF Ti-6Al-4V cellular metamaterials.

2. Methods

This section covers the material, the manufacturing conditions, the material characterization techniques, and the mechanical testing

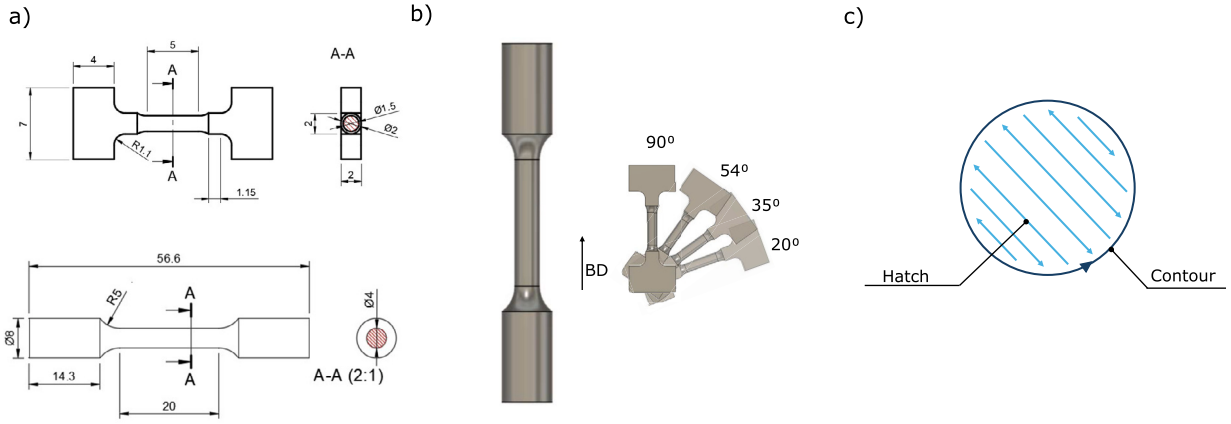

Fig. 2. a) the geometry of the net-shape struts (in mm), and the geometry of the vertical bulk sample, b) Sample inclinations considered in this study, c) schematic sketch of the scan strategy used.

Table 1
Composition of the Ti-6Al-4V powder.

Element	Ti	Al	V	Fe	O	C	N	H
Mass (%)	Bal.	6.3	4.0	0.21	0.09	≤ 0.01	0.01	0.001

methodology used during the study. Furthermore, the details on the finite element modelling used to rationalize the experimental results are detailed as well.

2.1. Material and manufacturing

2.1.1. Material

The material chosen for this analysis is a Ti-6Al-4V powder provided by Carpenter Additive®. The nominal composition is reported in Table 1. The particle size range distribution measures 14.9 μm (D10), 30.1 μm (D50), and 53.6 μm (D90).

2.1.2. Processing parameters

The process parameters (power, scan speed, hatch distance) to manufacture the samples were varied to study the accuracy of the different characterization techniques and the impact of the morphological features on the mechanical properties of the elemental struts compared to their large sample counterparts. Two different parameter sets using high (HSS) and low (LSS) scan speed, respectively, were chosen as indicated in Table 2. All the samples were manufactured with an Aconity Mini (Aconity GmbH, Germany) equipped with a 400 W infrared laser using a 30 μm layer thickness, 1 l/min Argon (>99.999% purity) gas flow, and an oxygen level below 200 ppm. The variable process parameters used to print the different sets of struts are detailed in Table 2. An inside-out hatch contour scan strategy using a 67° rotation at each layer was selected. All samples manufactured were heat treated at 800 °C for 4 h in a vacuum furnace (pressure $< 10^{-3}$ $mbar$), followed by furnace cooling to promote the formation of a $\alpha + \beta$ lamellar microstructure and relieve stresses on the samples [16]. No α-case was observed after the heat treatment following the Scanning electron microscope (SEM) evaluation.

2.1.3. Sample size

Two different sample sizes are studied to evaluate the effect of size on the microstructure, defects, geometrical deviation (measured as the difference between the nominal and actual specimen dimensions), and mechanical properties. Initially, a dog-bone specimen with a diameter of 4 mm is utilized, representing bulk material as shown in Fig. 2. Subsequently, a net-shape specimen with a constant strut size of 1.5 mm diameter was manufactured, and it represents the strut geometry used in lattice structures. The details of both geometries are presented in Fig. 2a.

2.1.4. Strut orientation

Previous studies widely recognize the effect of orientation on the defects and geometrical deviation of strut specimens [16,17,15]. For this reason, the orientations of 90° (vertical), 54°, 35°, and 20° were selected considering previous studies investigating lattices and single struts [22,13,17,14,23,16,24], as shown in Fig. 2b. The bulk samples were printed only at 90° to address the size effect. No supports were placed in the samples' gauge length at any orientations (Fig. 2b) to simulate the lattice's service conditions.

2.2. Sample characterization

2.2.1. Microstructural characterisation

To characterize the microstructure, samples were mounted longitudinally on bakelite, then ground and polished to colloidal silica. Afterward, standard Kroll's reagents were used to reveal the microstructure. For the case of the prior-β grain microstructure, the samples were analyzed using optical microscopy with an Olympus GX53. High-resolution scanning electron microscopy was used to analyze the $\alpha + \beta$ microstructure of the 90° samples for both strut and bulk specimens. The analysis was performed using a Hitachi S-3400N SEM microscope at a 10 kV beam voltage at a x3200 magnification using secondary electrons.

2.2.2. Geometrical deviations and internal defects characterization

To analyze the geometrical deviation of the actual strut cross-sectional area against the nominal one, three different measurement and characterization techniques are used in this work, as indicated in Fig. 3: standard linear measurement, optical microscopy, and CT scanning. The measurements obtained from all these techniques have been compared and rationalized carefully, exposing the importance of accounting for the correct load-bearing area in strut printed samples. Furthermore, this analysis addresses the key role of surface roughness in reducing weight in lattice structures, improving their mechanical properties, and the characterization of the difference in porosity observed between samples printed at different sizes and orientations.

The methodology employed for each technique is presented next:

- **1D linear measurement**: In this approach, a flat-end digital micrometer was used to measure the cross-sectional diameter of the net-shape struts and the bulk samples after the heat treatment without any additional post-processing. The average of three different diameters was considered to calculate the cross-sectional area of the struts.
- **2D optical microscopy imaging**: Two different image-based methods were used to analyze both struts and bulk samples: a destructive method using the sample cross-section and a non-destructive method using multiple longitudinal images of the samples' gauge

Table 2
LPBF processing parameters used for the manufacturing of the struts and the bulk specimens.

ID	Hatch Parameters			Contour Parameters			Energy density
	Power (W)	Scan Speed (mm/s)	Hatch distance (μm)	Power (W)	Scan Speed (mm/s)	Hatch distance (μm)	(J/mm^3)
HSS	150	2325	49.1	170	1600	80	43.7
LSS	150	1362	55.6	170	1600	80	66.0

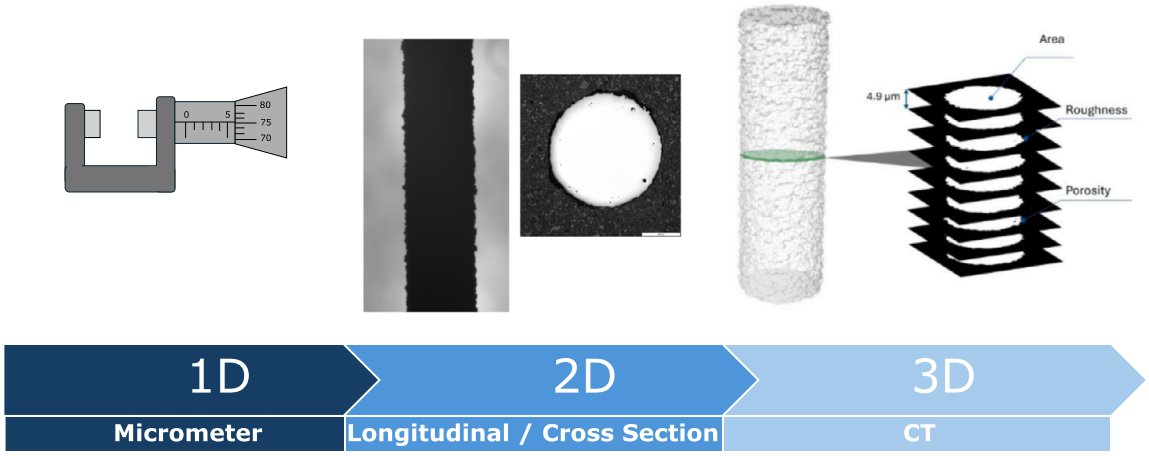

Fig. 3. Methodologies used in this study to evaluate the load-bearing area and geometrical deviation in Ti-6Al-4V struts.

length. The cross-sectional images of the samples were taken with an Olympus GX53 optical microscope following a metallographic preparation that involved an initial grinding step using up to a 1200-grit abrasive paper, followed by a polishing stage up to a 3 μm diamond suspension and a final step with colloidal silica suspension solution mixed with H2O2 (70:30). Three cross-sections per sample condition were analyzed to increase statistical relevance. As shown in Fig. 4, image analysis was used to binarize the image to calculate porosity (Fig. 4b) and successively extract the sample contour to measure the cross-sectional roughness (R_a^{CS}), and load-bearing area from the analyzed sections (Fig. 4c). The second methodology proposed is a non-destructive technique that consists of taking longitudinal images of the struts following the approach introduced by Dallago et al. [25] and adapted by Murchio et al. [17] to measure the area of elemental struts. Two longitudinal images of each sample, each rotated by 90°, were taken using a FLIR ® Blackfly S camera with a 12 megapixels resolution. Fig. 4d-f shows that the same image analysis steps were used to extract the surface features. In particular, longitudinal upskin ($R_a^{L\text{-}US}$) and downskin roughness ($R_a^{L\text{-}DS}$) were considered for this analysis. The load-bearing area was calculated assuming an elliptical cross-sectional area that uses the average strut thicknesses extracted from the two perpendicular longitudinal images as the major and minor axes.

- **3D X-ray computed tomography** (only for strut samples): An ImageiX CT system (North Star Imaging Inc.) was used to perform the CT analysis of the miniaturized struts. The analysis was performed using a 100 kV tube voltage, 40 μA tube current, and 5 μm focal spot size. A voxel edge length of 4.9 μm was achieved. A gauge length of 5 mm was characterized by 3600 projections with a 1 fps framerate. Dragonfly 2022.2 [26] was used to analyze the samples. One strut of each parameter per build orientation was analyzed. Post-processing algorithms were applied to denoise and enhance the image's sharpness. The Otsu threshold segmentation was applied to analyze the data [27]. Pores made up of fewer than 8 voxels (2x2x2) were filtered out of the segmented data, following the approach introduced by Du Plessis et al. [28] to eliminate noise from the measurement. The load-bearing area was defined as the average cross-sectional area of the strut's gauge length.

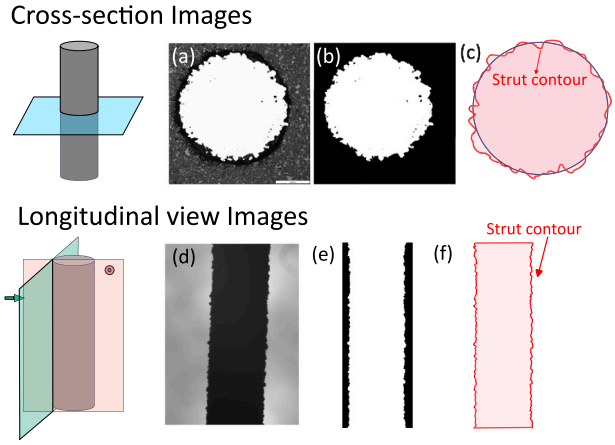

Fig. 4. The characterization of the Ti-6Al-4V samples is divided into cross-sectional and longitudinal analysis: a,b,c) the analysis workflow for cross-sectional images and d,e,f) the analysis workflow for longitudinal images.

2.2.3. Surface roughness

The surface roughness was calculated in two different ways: from the sample cross-section (R_a^{CS}) and from the longitudinal section ($R_a^{L\text{-}DS}$), extracting the data as indicated in Fig. 4c and 4f, respectively. Equation (1) shows the calculations used to determine the average surface roughness (R_a), following a similar approach to that proposed by Solberg et al. [29] for $R_a^{L\text{-}DS}$ and Hossain et al. [15] for R_a^{CS}. In longitudinal specimens, in order to compute the average surface roughness ($R_a^{L\text{-}DS}$) from surface profiles, the specimen waviness was removed by normalizing the outermost profile with respect to the sample centerline, defined as the average of the upper and lower profiles. Once the waviness was removed, the R_a was calculated according to Eq. (1) as defined in ISO 4287 [30].

$$R_a = \frac{1}{n}\sum_{i=1}^{n} | y_i | \tag{1}$$

where n is the total number of points, and y_i is the distance from the mean line at the i_{th} point. For strut specimens, both the CS and the LS

Table 3
Comprehensive test matrix summarizing the mechanical testing and characterization techniques employed in this study. All the samples considered in this study were analyzed in net-shape condition.

Sample type	Diameter (mm)	Orientation (°)	LPBF param.	Microstructure Charact.	Porosity	Roughness	Mechanical Tests
Strut	1.5	90, 54, 35, 20	HSS, LSS	SEM	OM, CT	OM, CT	Tensile
Bulk	4	90	HSS, LSS	SEM	OM	OM	Tensile

roughnesses were extracted from optical images and the CT data. Due to the reduced dimensions of the specimens, strict adherence to ISO standard guidelines for surface roughness measurement was not feasible. For this reason, a sampling length of 4.5 mm was uniformly applied for all longitudinal measurements. While this deviation may affect the absolute surface roughness values, the primary objective of the surface roughness measured from OM surface profiles was a comparative analysis across all the different specimen conditions. Therefore, the approach adopted was considered acceptable for the purposes of this study.

2.3. Mechanical testing

The tensile mechanical properties of the strut and bulk specimens were measured at room temperature using a universal tensile testing machine at a 10^{-2} 1/s strain rate controlled by a Linear Variable Differential Transformer (LVDT). Digital Image Correlation (DIC) was used as a virtual extensometer to measure the strain, as it is widely reported to measure surface strain more accurately than traditional extensometers [21]. A 5 mm gauge length was considered for these calculations. Images were taken using a FLIR ® Blackfly S camera with a 12 megapixel resolution at 10 fps. The load-bearing area considered to calculate the YS and the UTS of the struts is discussed in the result sections. The yield stress was determined using the 0.2% offset method, by intersecting the stress-strain curve with a line parallel to its initial linear portion, with an offset of 0.2% in engineering strain. Three repeats per condition were tested. A comprehensive test matrix summarizing the mechanical and microstructural characterization conducted on the samples is presented in Table 3.

2.4. Finite element analysis

A Finite element analysis (FEA) was performed using ANSYS Mechanical 24.1 ® software to study the load distribution of the as-built geometry in miniaturized struts under quasi-static tensile testing conditions. Quadratic tetrahedral (Tet10) solid elements were used to mesh the CT-derived gauge length geometry of the HSS and LSS sets, respectively. An adapted LPBF Ti-6Al-4V material model from the literature was used in the simulation [31]. A displacement along the Z-axis on one extremity of the gauge length and pinned nodes on the Z-axis on the opposite side were applied to simulate the tensile testing boundary conditions of the strut gauge length.

2.5. Fractography

After testing, the fracture surfaces of the vertically manufactured strut and bulk samples were analyzed using a Hitachi S-3400N scanning electron microscope (SEM). Fracture surface images were taken at a beam voltage of 15kV and a magnification of x50 for the global strut images to compare the load-bearing area and x450 to analyze the fracture details.

3. Results and discussion

This section presents and discusses the results obtained investigating the impact of the feature size on the material and mechanical properties of LPBF Ti-6Al-4V by comparing strut samples with lattice structures-like characteristic size with bulk samples. Furthermore, the influence of processing parameters on the size effect and the impact of orientation in strut specimens are considered.

To achieve this objective, first, the effect of size and processing parameters on the microstructure is analyzed. Then, the impact of size, processing parameters, and printing orientation on the porosity and roughness is rationalized using the different characterization technologies outlined in the methodology.

Then, the role of the load-bearing area in calculating mechanical properties is addressed by comparing the mechanical performance of the bulk Ti-6Al-4V samples with the strut ones. A FE analysis of the CT scanned geometries was performed to highlight the different stress distributions and propose the actual load-bearing area obtained from the struts manufactured with the two process parameter sets. Finally, based on the results, some implications to the mechanical design of lattice structures are presented.

3.1. Microstructure

The influence of sample dimensions and processing parameters on the microstructure of the Ti-6Al-4V samples was compared both along and across the building direction to highlight any differences. The microstructural images are presented in Fig. 5.

In terms of the α lath microstructure, Fig. 5a-b-e-f presents the high-magnification lath microstructures obtained via SEM of the transverse cross-sections for both the strut samples (a-b) and bulk samples (Fig. 5e-f). The heat-treated microstructure of the struts in Fig. 5a,b is characterized by a typical basketwave structure with the white lamellae representing the β phase [32,33]. To study the difference between the lath thickness of these microstructures, a two-way ANOVA followed by a Tukey's Test ($p < 0.05$) was used, using a sample of 150 laths. As shown in Fig. 5i a statistically significant difference was observed between HSS and LSS parameter sets, having an average α lath thickness of 1.07 ± 0.36 μm and 0.90 ± 0.26 μm for HSS and LSS parameter sets, respectively. This discrepancy is derived from the difference in melt pools produced by the two sets of process parameters used. As observed from single tracks on bulk experiment using HSS and LSS process parameters (Fig. 5c-d), it is evident that LSS parameters achieve a stable melt pool indicative of conduction mode, while HSS parameters show signs of balling and melt pool instability as demonstrated by the spherical droplet formed atop the melt pool. This is in agreement with the results obtained by Cepeda-Jiménez et al. [33], which shows that higher stability ultimately results in a smaller driving force for grain growth during the heat treatment, producing finer laths [33]. These microstructural differences will be linked later with the mechanical properties observed. For the case of the bulk samples, a comparison of the microstructures obtained is shown in Fig. 5e-f. A similar basketwave lamellar microstructure is observed, however, the lath thickness presents a statistically significant increase in the average lath thickness to 1.26 ± 0.43 μm for HSS and 1.19 ± 0.41 μm for LSS condition, which represents an 18.0% increase for HSS and a 33.3% increase for the case of LSS. This trend, previously reported in other studies [13,14], has been linked to the refinement of the prior β grain size and differences in thermal history during the processing and heat treatment between large and small samples. These changes will be further discussed in the mechanical section, rationalizing the observations on the mechanical properties of both-size samples. In bulk samples, the difference between HSS and

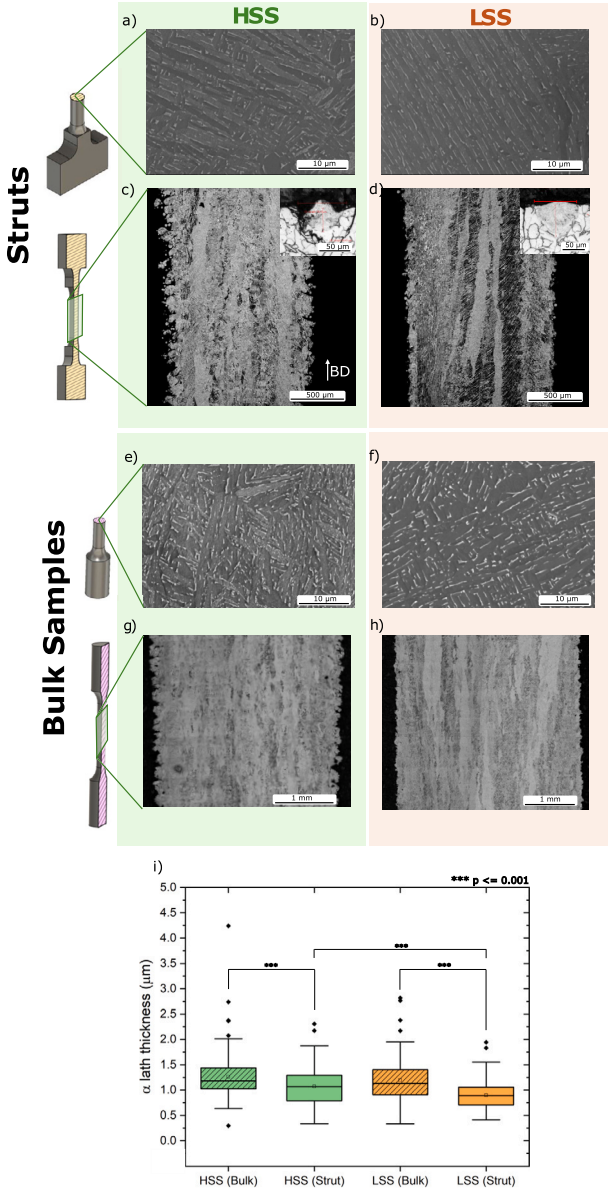

Fig. 5. The microstructure of struts (a,b,c,d) and bulk (e,f,g,h) samples for both HSS and LSS parameter sets. SEM high-magnification micrographs of the transversal cross-section for struts (a,b) and bulk (e,f). Low-magnification OM etched micrographs of the longitudinal cross-section for struts (c,d) and bulk (g,h) samples. The average α lath thickness for both HSS and LSS conditions in struts and bulk is shown in (i).

LSS parameter sets was found to be not statistically different, which is likely due to the slower cooling rates, which allow for more homogenization in the microstructure compared to smaller struts [34].

On the other hand, the prior-β grains structure was revealed through etched longitudinal sections, and is presented in Fig. 5c-d-g-h. Although OM does not provide information on crystallographic texture, it can still offer valuable insights into the topology of the prior-β grains, which can be inferred from the arrangement of α-lath colonies within them. In fact, a tendency to form columnar grains is observed along the building direction, which several authors have reported before [2,35,36,33]. A qualitative analysis based on OM also suggests that variations in the processing conditions influence the dimension of the prior-β grains, as observed for both the strut and bulk samples. The samples manufactured at a high scan speed (HSS) exhibit shorter prior β grains compared to those printed with low scan speed (LSS), which show larger and longer grains aligned with the building direction of the sample. This phenomenon can be explained by the difference in melt pool stability between the parameter sets. As mentioned in the context of α lath, the lower E_v used for HSS produces a smaller and more unstable melt pool. On the other hand, a higher E_v leads to a deeper and more stable melt pool in conduction mode, which, due to directional thermal gradients and higher re-melting, promotes the epitaxial growth of prior β grains [33]. However, further analyses using Electron Backscatter diffraction (EBSD) are required for a more detailed comparison.

3.2. Porosity

Porosity plays a critical role in the mechanical properties of LPBF parts. Its minimization is usually the main criterion for assessing the quality of a component. The effect of porosity is even more critical in strut specimens as its larger pore-to-volume ratio increases the risk of premature failure under loading and can modify the load-bearing area of the sample. Therefore, understanding the effect of size employing a characterization method that accurately captures the porosity is essential. Fig. 6 compares the porosity results (expressed as percentages) obtained using optical microscopy analysis of the cross-sections of both the bulk and strut samples. The effect of the processing parameters and printing orientation are also included. For the case of the struts, the results are compared to the ones obtained using CT scanning for correlation.

The first observation is that bulk samples consistently exhibit lower porosity than their miniaturized counterparts. This can be produced by the size effect stemmed by the larger cross-sectional area, which leads to a different thermal history of the parts, leading to a more stable process that minimizes the defect formation [37]. On the other hand, large samples printed with HSS present a higher porosity than those printed with LSS. This can be attributed to a higher prevalence of lack of fusion defects due to the reduced energy density input achieved by manufacturing struts at higher scan speeds [38,39]. The same tendency is observed in strut samples, where HSS shows higher porosity independently from the strut orientation.

In strut samples, porosity strongly varies with printing orientation: this variation is partially attributed to the differences in thermal conductivity between powder and solid materials, which change the thermal profiles at higher strut inclinations affecting the heat dissipation [40,41], and partially to the different slicing of the strut geometry at various inclinations that influences the length and interaction between hatch and contour scan vectors [42,43]. This produces a maximum porosity at mid-inclinations of the orientation of the struts.

Compared to 3D computed tomography, 2D OM porosity analysis tends to overestimate porosity. For the case of the HSS strut set, there is an error of 122%, compared to the 102% observed in the LSS set. One of the differences between the characterization methods lies in the misclassification of some open pores due to the strut's roughness, as illustrated in Fig. 7. In 2D cross-sectional porosity analysis, all the porosity, including the one near the surface, is categorized as closed. However, after analyzing multiple sections, it is shown that some pores near the surface should be considered open. During CT analysis, this open porosity is discarded, leading to more precise closed porosity measurements. In any case, it is important to note that while the CT analysis measures the porosity of the entire gauge length of the strut, the 2D OM approach only provides an approximate value derived from the average porosity observed across three cross-sections.

When investigating porosity, the overall porosity fraction is not the only important factor. For example, the fatigue performance of a sample depends heavily on the pore size and their distribution [44,17]. Therefore, it is critical to characterize it accurately. For this reason, the pore size distribution for each material condition has been calculated and presented in Fig. 8. The spatial distribution observed in the CT scans of the strut samples shows that most of the porosity is concentrated at the hatch-contour interface. This is likely due to the mismatch between the hatching and contour vectors, as previously reported in the literature. [16,45]. This phenomenon contributes to explaining the reason behind

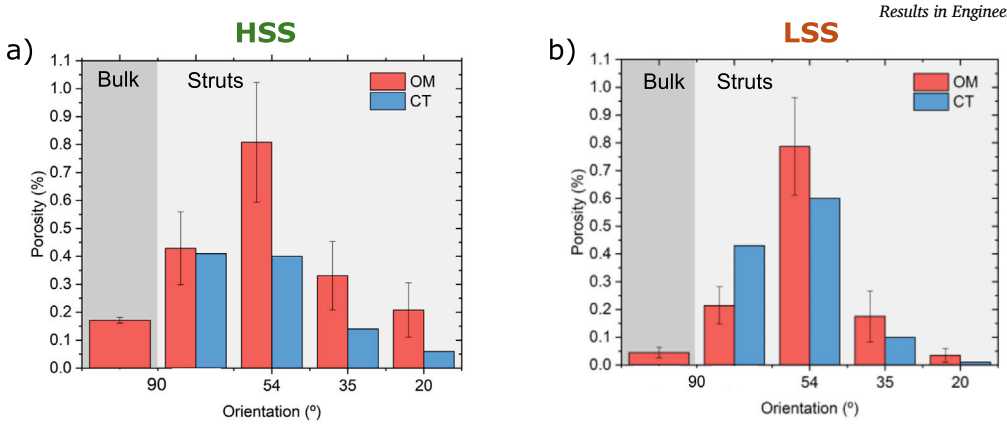

Fig. 6. Porosity analysis of a) HSS and b) LSS sets of bulk and miniaturized Ti-6Al-4V samples comparing the 2D porosity obtained through optical microscopy and the 3D volumetric porosity percentage obtained via CT.

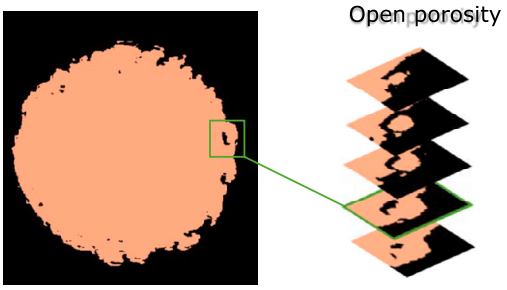

Fig. 7. An example illustrating the limitations of 2D OM characterization in its tendency to misclassify open porosity. When analyzing multiple consecutive cross-sections, as made possible by CT, it becomes evident that some close pores are, in fact, open. This occurs due to the roughness of the sample affecting the porosity profile.

the bulk samples' overall lower porosity level compared to struts, as the hatching-contour interface is relatively smaller (in percentage) due to the lower surface-to-volume ratio.

It is important to note that when comparing the porosity extracted with both techniques, several factors must be considered: in 2D porosity, the pore intersects by a plane, and its dimensions are measured accordingly. This results in an underestimation of the pore's actual diameter as the cutting plane rarely intersects the pore at its largest dimension [46]. In fact, as evidenced by the statistical results in the Appendix, the median, mean, and, in particular, the maximum pore size measured by CT are consistently larger compared to those measured by OM, resulting in statistically significant differences across all cases analyzed ($p>0.05$). Secondly, the CT presents some limitations in the measurement of small pores as observed by the distributions in Fig. 8. This is due to the fact that CT scanning presents a resolution threshold defined by the machine the material used, and the volume scanned, which prevents the characterization of the smallest strut pores. Lastly, despite the wide use of this technique to calculate the porosity [41,46,47,38,48,49] the impact of the statistical relevance of the OM cross-sectional analysis needs to be accounted for. When fewer larger pores are present in the sample, as in the HSS strut at 20° (Fig. 8a), 2D OM porosity provides limited statistics on the actual sample porosity. On the contrary, in a sample with uniform porosity, few cross-sections can provide an insightful representation of the overall porosity of the sample, as observed for the cases of HSS and LSS struts inclined at 54°.

3.3. Surface roughness

Surface roughness is a critical aspect when additively manufacturing metal parts as it strongly influences the mechanical properties through premature failure of the material. This is even more acute for small-size specimens, such as struts, where the relative effect is higher. For this reason, an in-depth assessment of the surface quality of the sample is fundamental, given the limited ability to post-process the struts in most lattice structures and the consequent influence that surface roughness has on mechanical properties [14,50,17,15]. Fig. 9 shows the results obtained considering average roughness for the cross-section and longitudinal analysis of the surface profiles using both OM and CT data.

In the cross-sectional analysis (Fig. 9-top), in terms of the processing parameters effect, the HSS set present a higher R_a^{CS} compared to the LSS set. This is due to the higher scan speed used to manufacture the sample. This difference is more than three-fold when comparing the R_a^{CS} of the vertical samples. In terms of the size effect, unlike porosity, cross-sectional roughness measured in bulk samples is consistent with the values obtained in the corresponding strut samples. This indicates that the roughness is influenced mainly by the process parameters but is mostly independent of the sample size at the same orientation. However, similar roughness values do not imply a similar effect of the roughness on the mechanical properties. As the sample size decreases, roughness remains constant, while the sample volume decreases, increasing the detrimental effect on the strut specimens. This will be further discussed in the mechanical properties section. Finally, in terms of the orientation, the downskin roughness of the samples manufactured with both process parameters increases with increasing sample inclination, as highlighted in the longitudinal analysis below.

The observed difference in downskin roughness was measured through the longitudinal analysis (Fig. 9-bottom) of the samples. Only the downskin roughness was considered, as it is widely reported to be the most critical for mechanical properties [51]. As shown in Fig. 9, the downskin roughness of HSS and LSS samples have a difference similar to the one reported above for cross-sectional roughness, and is comparable between bulk and strut samples. Lastly, the samples' orientation has a major effect on the downskin roughness, which increases with increasing inclination of the strut specimens due to the dross phenomenon, which causes excessive melting on the bottom side of the strut due to increasing contact with the metal powder, which presents a significantly lower thermal conductivity [52,51,16,24] compared to the solid material. Consequently, an increase of 117% and 232% in $R_a^{L\text{-}DS}$ was measured for HSS and LSS samples, respectively, when comparing 90° struts to 20° ones.

The results show that the deviation between the two measurement methodologies used in this study is notably higher in the HSS set. For the case of the cross-sectional analysis, on average, the 2D imaging method results in roughness values that are ≈ 42% higher compared to CT. In contrast, the values measured with OM on the LSS set only overestimate the CT values of 16.6%, on average. For longitudinal analysis, the deviations between OM and CT of the two sets are 18.9% for HSS and 9.5% for LR, presenting a significantly lower deviation between the two characterization methods as observed in a 1-to-1 roughness profile comparison

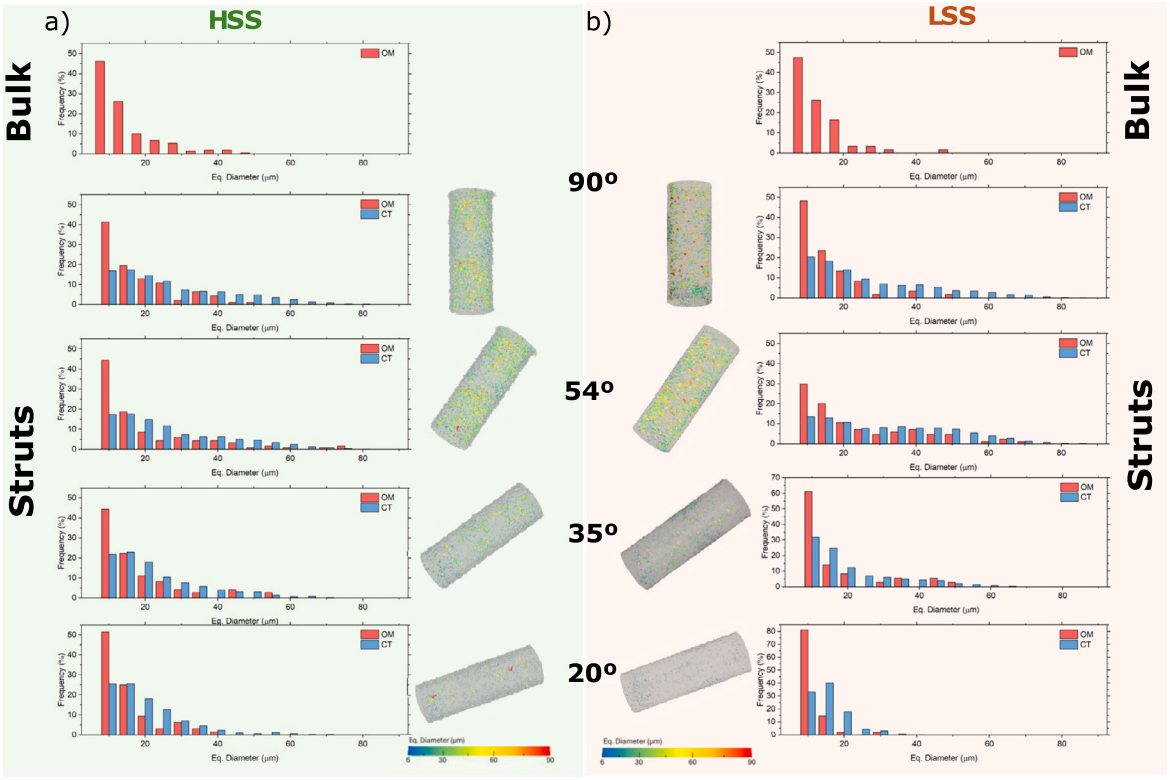

Fig. 8. Porosity size distribution analysis of a) HSS and b) LSS struts at different orientations. A comparison between the results obtained via OM and CT is presented. In addition, using CT, the internal voids in the gauge length of the struts are displayed to provide a visual comparison of the spatial pore distribution. When comparing CT and OM, the p-values for all cases, regardless of orientation or processing parameters, were found to be < 0.05, indicating statistically significant differences between the distributions.

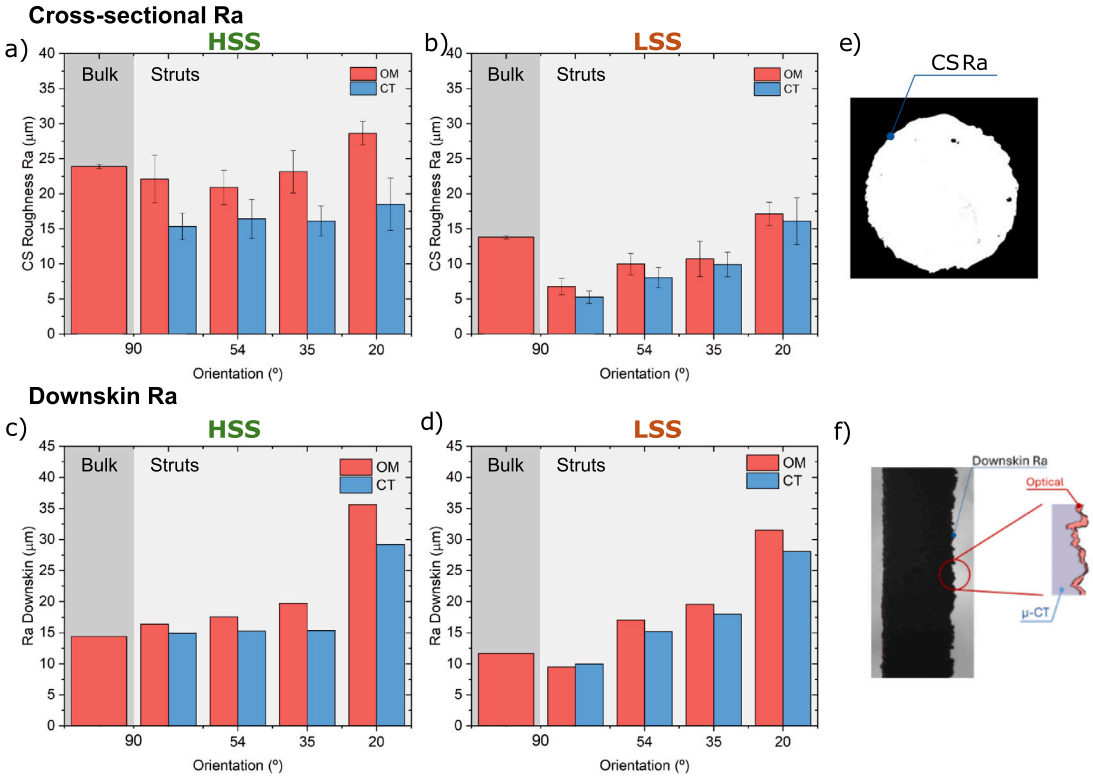

Fig. 9. Top: Cross-sectional roughness analysis: R_a^{CS} analysis of a) HSS and b) LSS sets measured using 2D OM imaging and CT. Bottom: Longitudinal roughness analysis: $R_a^{L\text{-}DS}$ analysis of c) HSS and d) LSS sets measured using 2D OM imaging and CT. e) Binarized cross-sectional area of the strut used to calculate R_a^{CS} f) 1-to-1 roughness profile comparison calculated using 2D OM and CT. Results obtained for bulk samples were obtained using 2D OM.

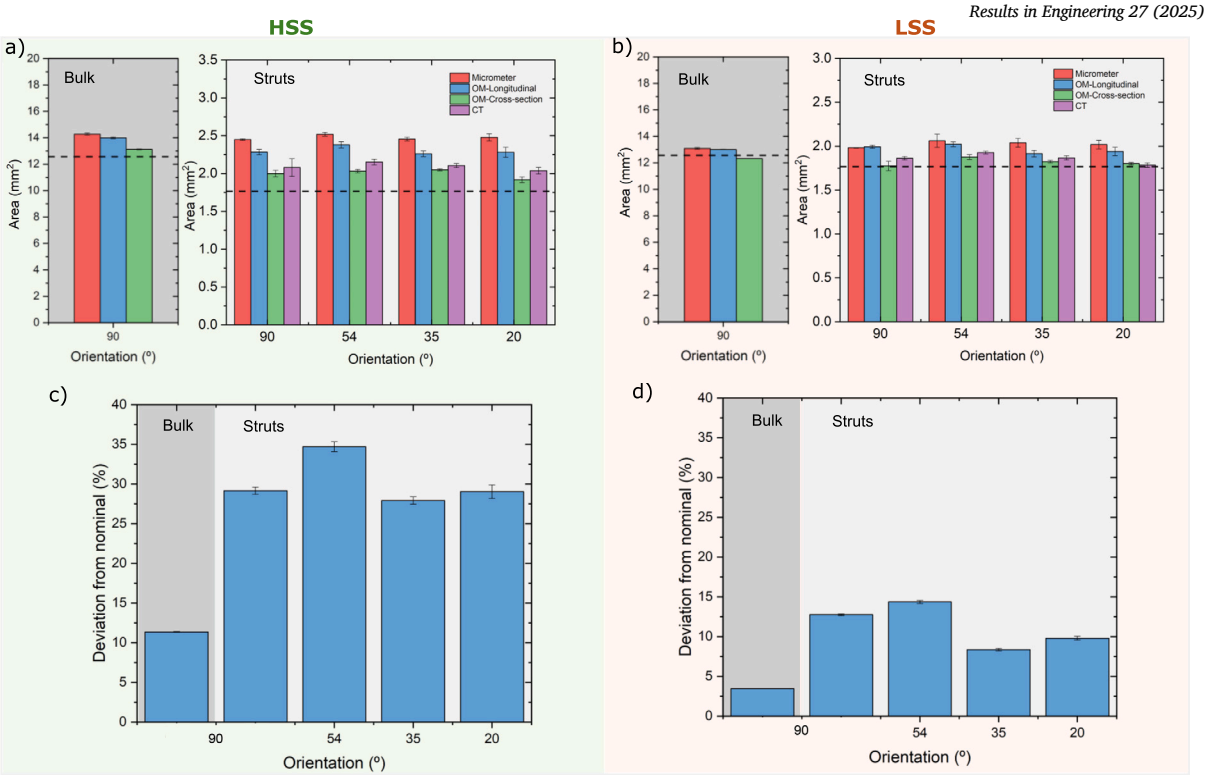

Fig. 10. Influence of the sample size, processing parameters, and orientation on the cross-sectional area using different characterization methods (top) and deviations from the nominal area designed (bottom). The reader is referred to the appendix section for details on the calculation of the corrected cross-sectional area estimated from longitudinal images.

for the LSS 20° strut in Fig. 9f. The complete set of results regarding the differences encountered between methodologies can be found in the Appendix. The main factor determining the difference between the two methods is the limited resolution of the CT imaging, primarily due to the voxel size. Although image post-processing techniques were employed to enhance image sharpness, the comparable magnitude between voxel size and surface roughness limits detailed evaluations requiring higher resolution for more accurate results. However, achieving higher resolution requires significantly longer scan times associated with increased costs [28]. On the other hand, based on the obtained results, it is shown that 2D optical microscopy is proven to be a reliable method, even at low magnification, to measure the surface roughness of a sample efficiently.

3.4. Geometrical deviations

The effects of sample size, processing parameters, and sample orientation on the geometrical deviations of the manufactured samples with respect to the nominal CAD geometry were analyzed using various characterization methods, namely (i) digital micrometer, (ii) longitudinal 2D OM approach, (iii) cross-section 2D OM approach, and (iv) CT (only for struts). The results of the estimated area using the different methodologies are presented in Fig. 10a-b. To facilitate the analysis of the effect of the sample size, the area deviations obtained from the 2D longitudinal OM (technique common to all samples) were evaluated against the nominal target value as illustrated in Fig. 10c-d. The reader is referred to the appendix for details on the calculation of the corrected cross-sectional area estimated from longitudinal images and the rationalization describing the reasons for this significant difference between the methodologies used.

In terms of the effect of the methodology used, as observed across the different sizes, orientations, and process parameters in Fig. 10a-b, the measured areas differ depending on the methodology used. For instance, the 2D longitudinal OM approach approximates the sample area as an ellipse using Feret diameters from projections, which is more accurate than the micrometer but still overestimates the actual area. However, since it considers the entire gauge length, it provides a representative and non-destructive measurement method. On the other hand, the 2D cross-sectional approach systematically underestimates the area calculated from the CT, which is considered the ground-truth data in strut samples as the struts analyzed in this study [20]. The significant differences between the methodologies are schematically presented in the corresponding section of the appendix. The implication of these discrepancies between methodologies indicates the critical need to accurately measure the sample, in particular the struts load-bearing area, to obtain reliable mechanical properties. This will be further discussed in the following section.

In terms of the effect processing parameters, independently of the characterization technique used, all manufactured struts present a larger load-bearing area than the nominal CAD design. This is attributed to the process parameters used, in particular, the scan speed, the offset of the contour vectors, and the laser delay parameters [53,16]. The effect of the process parameters, mainly scan speed, is evident, as LSS samples present smaller areas when compared to HSS. This is directly attributed to the higher surface roughness of the HSS samples, which overmelt the material beyond its nominal boundaries. In terms of the effect of the sample size, the deviation from the nominal area presented in Fig. 10c-d shows that as the sample size decreases, the deviation increases. Bulk samples exhibit a 17% and 9.3% lower deviation for HSS and LSS, respectively, compared to their strut counterparts. This is due to the fact that, as shown in Fig. 9, the roughness of bulk samples is comparable to the ones of struts, which notably decrease its impact on the deviation from the nominal CAD dimensions as the sample area increases. Finally, in terms of the effect of the printing orientation, the results show no clear linear trend as the deviation fluctuates across different printing orientations. While higher inclinations lead to increased downskin roughness due to overmelting from the different thermal history, this ef-

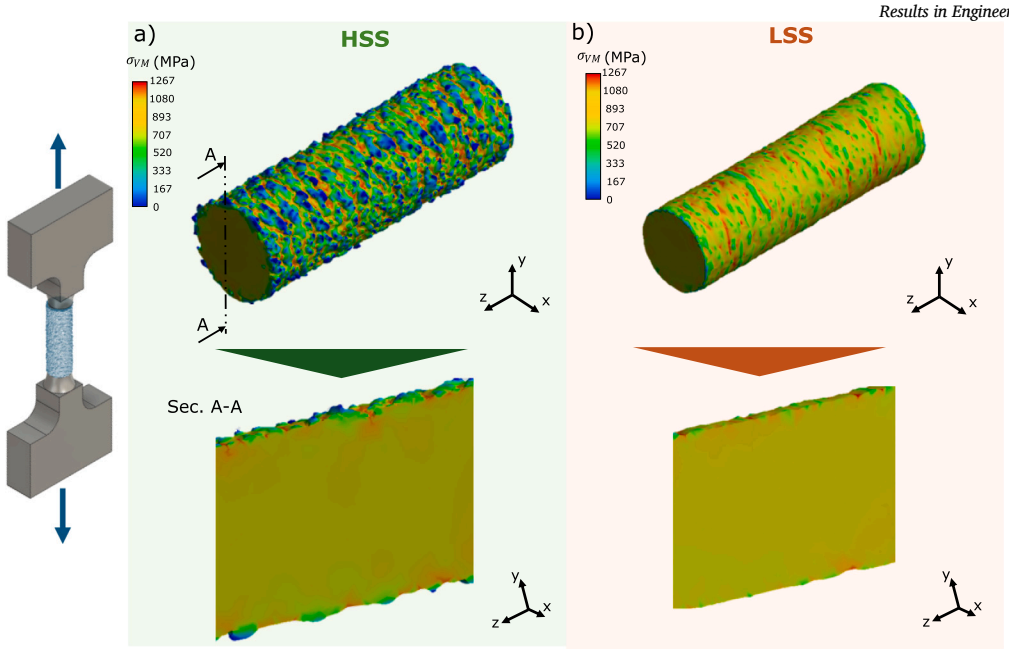

Fig. 11. The Von Mises stress state calculated from the FE analysis for the a) HSS 90° strut, and b) LSS 90° strut at yielding.

fect is counterbalanced by mass loss at the lateral sides, a phenomenon commonly observed when printing inclined round struts. [54,17].

3.5. Mechanical behaviour

In this section, the mechanical properties of the material are analyzed, including the effect of size and orientation of the sample, along with the influence of the processing conditions. The mechanical properties are extracted from uniaxial tensile test in the form of stress-strain curves. To calculate the intrinsic stress of the material, the load-bearing cross-sectional area of the specimen needs to be assessed accurately. This is critical in strut specimens, as roughness and slight deviations can considerably alter the load-bearing area, distorting the mechanical properties measured. For this reason, this part of the study starts with a careful assessment based on computational simulations of the load-bearing area of the specimens depending on the printing parameters, size, and part orientation. Then, those areas are used to assess the mechanical properties and understand the influence of size, orientation, and processing parameters on YS, UTS, and ductility.

3.5.1. Assessment of the load-bearing area of the specimens and the effect of surface roughness on strut specimens

The mechanical properties of the specimens are extracted from stress-strain curves, which depend on the load-bearing area of the specimens used for the experiments. As stated before, addressing the correct cross-sectional area of small specimens is not trivial, in particular due to the irregular surface roughness that can significantly alter the portion of stressed material and, therefore, the actual load-bearing area. To further investigate the effect of surface roughness and accurately assess the specimens' load-bearing area, finite element analysis (FEA) was used to simulate a tensile test of the actual reconstructed CT sample geometries. Simulations were performed for all the samples analyzed using CT scans. As a result, the equivalent Von Mises (VM) stress state under static loading for the 90° samples is presented in Fig. 11, as a comparison for a high and low roughness sample. The FEA of the LSS samples (Fig. 11b), shows that the stress state is homogeneous along the gauge length and the cross-sectional area up to the sample surface. That means that all the material is carrying stress and contributing to the load-bearing capacity of the sample. On the other hand, the FE simulation of the HSS strut specimens (Fig. 11a) exhibits a more heterogeneous stress state on its surface. The outer roughness features do not carry any stress while, the roughness valleys act as stress concentration features, notably inducing a stress increase by the edge of the cross-section as also described by Persson et al. [55]. The combined effects of the unloaded surface and the stress concentrations notches reduce the actual load-bearing area as the surface roughness acts like a series of closely spaced notches disrupting the stress flow, as shown by Pilkey et al. [56]. Given that the outer layer does not experience any stress, it is reasonable to assess that it should not be considered when estimating the sample's mechanical properties.

Table 4
The load-bearing area of the strut (A_{lb}) is calculated and compared with the area extracted from the CT measurement (A_{ct}).

	Orientation (°)	Area CT (A_{ct}) (mm^2)	Load-bearing area (A_{lb}) (mm^2)	A_{lb}/A_{ct} (%)
HSS	90	2.080	2.035	97.86
	54	2.152	2.049	95.22
	35	2.106	2.060	97.81
	20	2.038	1.935	94.95
LSS	90	1.863	1.853	99.51
	54	1.927	1.902	98.70
	35	1.866	1.853	99.32
	20	1.784	1.725	96.70

To quantify the load-bearing area in each of the processing conditions and orientations, the stress state at 10 different cross-sections per sample has been analyzed. Representative examples of these cross-sections are presented in Fig. 12. The central regions of the strut exhibit a homogeneous stress level (≈ 880 MPa); however, moving toward the sample surface, the stress initially mildly increases, followed by a sudden decrease. It was considered as a load-bearing area for each cross section, the area that is loaded with at least 50% of the average stress at the core of the sample. The results of the adjusted load-bearing area using FEA are presented in Table 4. The efficient load-bearing area is calculated as A_{lb}/A_{ct}.

The load-bearing areas assessed are in agreement with experimental observations extracted from the fractography images of the tested samples, which will be presented in the mechanical properties section. According to these results, the inefficient area accounts for the 3.5% on average of the total cross-sectional area in the HSS strut specimens, while it is only the 1.4% on average for all the LSS samples. These results

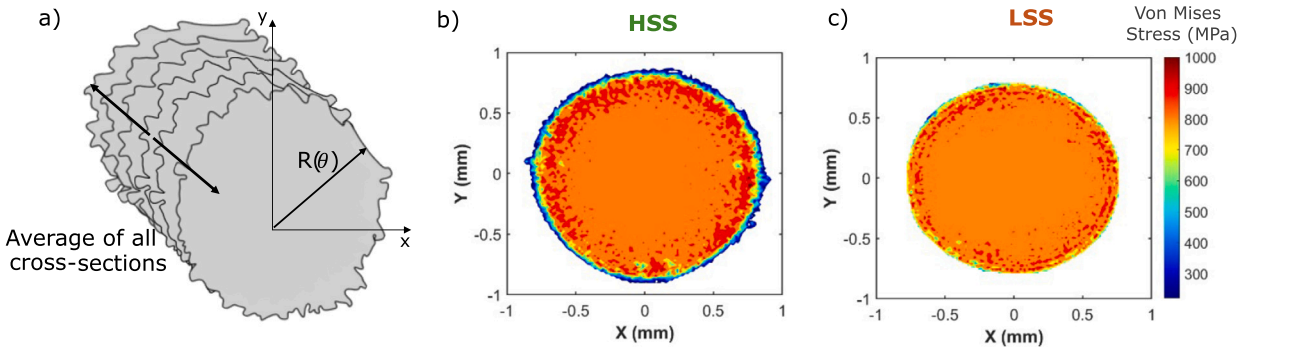

Fig. 12. a) The schematic view of the cross-sections used to perform the analysis of the efficient area. The contour plot of the average VM stress values for the HSS 90° b) and LSS 90° c) struts.

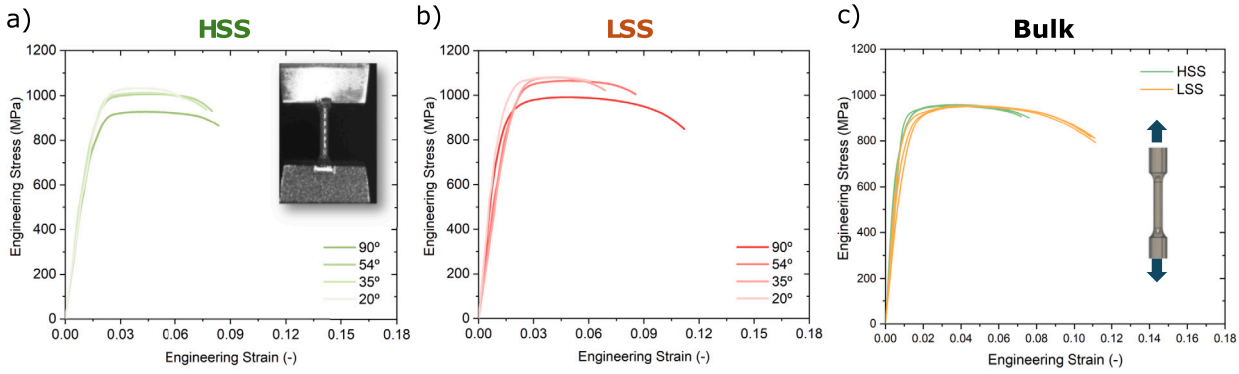

Fig. 13. Representative engineering stress-strain curves for each inclination of a) HSS and b) LSS struts. c) Engineering stress-strain curves obtained from vertically printed HSS and LSS bulk samples.

further highlight the importance of surface roughness on the efficiency and mechanical performance of the struts.

Furthermore, the impact of orientation is evident as shown in Table 4, as the strut becomes increasingly inclined in the horizontal direction, roughness increases and contributes to a reduction in the efficient load-bearing area of the tensile sample. This reduction directly affects the lightweight efficiency of lattice structures, as a larger portion of the mass does not contribute effectively to the load-bearing area, undermining one of the key advantages of these architectures. The effective load-bearing areas calculated here will be used in the following section to extract the material's intrinsic mechanical properties.

3.5.2. *Stress strain curves*

The stress-strain curves obtained from the tensile tests of both strut and bulk samples are reported in Fig. 13. The effective load-bearing areas estimated from the calculation in the previous section were used to calculate the stress. For bulk samples, YS and UTS were calculated using the load-bearing area extracted from 2D longitudinal OM, as the roughness-related uncertainty is reduced in bulk samples due to their larger dimensions. Specifically, a deviation less than 2% is observed when comparing the measurements obtained using the micrometer and the 2D OM approach, lower compared to the one observed in the struts.

The results highlight the increased mechanical properties of LSS struts compared to HSS ones and their bulk counterparts. Moreover, a significant change in the ductility as a function of the sample's orientation is observed. To quantify these effects, the mechanical properties of the specimens were extracted from the stress-strain curves, which are explained in the following section.

3.5.3. *Mechanical properties*

The yield stress (YS), the ultimate tensile strength (UTS), and the ductility are shown in Fig. 14. The YS and UTS values measured in this analysis are consistent with the ones calculated for bulk samples and those observed in other studies of AM Ti-6Al-4V miniaturized specimens [17,14,13,57]. The elastic modulus was not considered in this study, as previous studies [58,59] highlighted that tensile tests on miniature samples are more sensitive to external factors such as clamp effect and specimen alignment, which negatively influence the elastic modulus estimation, suggesting the use of ultrasound and thermomechanical tests as a valid alternative.

Initially, the impact of size on the mechanical properties is assessed. A comparison of the mechanical properties between bulk and strut samples indicates that, despite the similarities in surface roughness and reduced porosity levels, the UTS of bulk samples is statistically inferior ($p<0.05$) to that of the struts. This is attributed to the finer α lath size observed in struts, resulting from the higher cooling rates experienced by the struts compared to the bulk samples due to their lower thermal mass [13,14]. The similar UTS observed in HSS 90° strut specimens when compared to their bulk counterpart may be attributed to the higher stress-concentrations effect induced by the high surface roughness on the reduced strut volume, as previously rationalized in Section 3.5.1. Although a statistically significant difference ($p < 0.01$) exists between the UTS of strut and bulk samples, this is not the case for YS results, which exhibit higher variance. Therefore, the results obtained only provide an indication to strengthen the hypothesis shown by the UTS values; however, further tests would be required to confidently assess these results. The elongation at fracture in bulk samples is consistent with the corresponding strut one, and no statistically significant difference was measured, in agreement with the findings of June et al. [20], despite the bulk samples having lower porosity levels than struts. On the other hand, a significant change ($p < 0.001$) was observed between samples manufactured with different process parameters. This suggests that the primary factor contributing to the overall difference in elongation at fracture, independently of the sample size, is the surface roughness. As

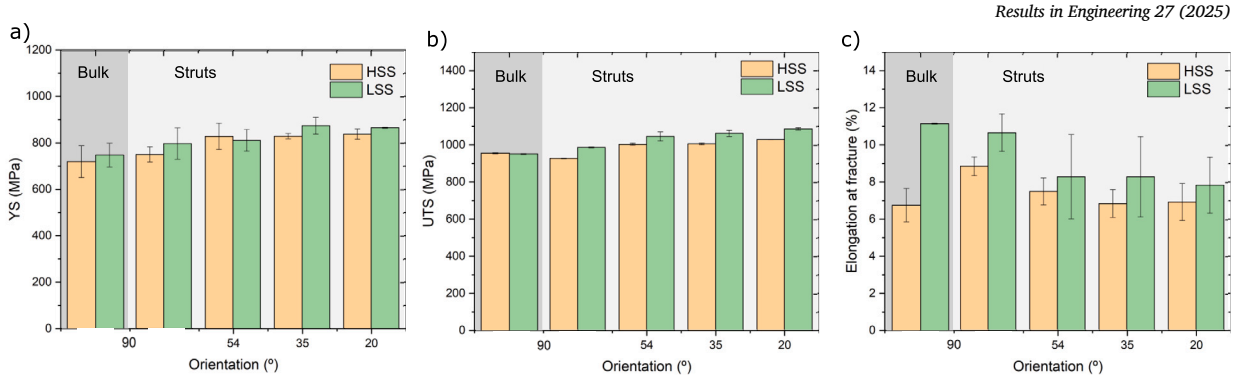

Fig. 14. The mechanical properties, namely the YS, UTS, and ductility of the HSS and LSS struts and bulk samples.

demonstrated by the FEA analysis surface roughness induces localized stress concentration that can promote early crack propagation. The results obtained from the tensile tests support this hypothesis in both strut and bulk samples. They also indicate that, for 1.5 mm struts, the size effect is minimal compared to bulk samples, suggesting that this effect becomes more pronounced at smaller sizes, as demonstrated in previous studies [13,16,50].

In terms of the effect of the printing orientation observed in the mechanical properties, the elongation at failure decreases approximately of 21% for HSS ($p<0.05$) and 26% ($p\leq0.05$) for LSS from vertical to 20° oriented struts. This is attributed to the sharp roughness increase observed at increasing inclination, as shown in Fig. 9. The highest values for the YS and the UTS of 875 MPa and 1088 MPa, respectively, are achieved at 35° and 20° for the LSS set. A subsequent decrease in the YS is observed at 20°, indicating non-monotonic relationship between the mechanical properties and the orientation [16]. This trend is attributed to a trade-off of the effects of microstructure, porosity, and surface roughness. In fact, while a porosity decrease is observed at higher inclinations, typically leading to an increase in mechanical properties [41,38,44], surface roughness (i.e., $R_a^{\text{L-DS}}$) at 20°, increases steeply (see Fig. 9). This increase might lead to higher stress concentration, ultimately promoting the earlier appearance of plastic deformation, producing lower yield stress as observed for LSS struts [14,60,50]. A further factor is the influence of microstructure on mechanical properties. Despite the α lath size not varying significantly across the orientations as shown in a previous study on Ti-6Al-4V struts [16], Zhang et al. [44] report that plasticity in Ti-6Al-4V struts manufactured at lower inclinations is promoted. This is due to higher proportions of grains with high Schmidt factor (considering the $\langle a \rangle$ prismatic slip plane in HCP), which have lower critical shear stress compared to those at higher strut inclinations. Additionally, the strong texture along the building direction which can be inferred from OM of the prior β grains, particularly in LSS struts as shown in Fig. 5d, can lead to a certain degree of anisotropy that can ultimately contribute to a difference in mechanical properties [61].

Finally, the influence of processing parameters on the mechanical properties is discussed. For the case of the struts, a comparison of the YS and the UTS between HSS and LSS strut specimens shows that, on average, the HSS samples have -3.2% YS and -5.4% ($p<0.001$) UTS, respectively. This is the case despite having similar porosity and pore size distributions for strut specimens printed at the same orientation. As discussed in Section 3.1, the microstructure shows a statistically different α lath size between LSS and HSS, with LSS exhibiting thinner laths, which may contribute to the higher YS and UTS measured, according to the Hall-Petch relationship. Nevertheless, the general similarity of the other microstructural features and defects suggests that surface roughness can be considered the dominant factor influencing the difference between the sample's mechanical properties, including elongation at fracture. At the same strut orientation, the mechanical properties systematically decrease with increasing surface roughness levels, similar to the trend observed with the elongation at fracture. This can be caused by high roughness, which promotes more crack initiators and induces higher stress concentrations, leading to premature failure of the samples [14]. For the case of bulk specimens, the difference in mechanical properties between HSS and LSS samples decreases, with the YS of LSS bulk samples being 3.89% higher and the UTS -0.4% lower than HSS bulk samples. This can be attributed to (i) the contained α lath size gap between LSS and HSS conditions, (ii) the lower porosity levels in both samples, and (iii) the reduced impact of surface roughness relative to the sample size. At the same time, elongation at fracture is consistent with the results obtained for strut specimens with $11.15 \pm 0.03\%$ for LSS and $6.78 \pm 0.89\%$ for HSS. This is attributed to the difference in porosity levels (higher in HSS than LSS bulk samples) and surface roughness between the sample conditions. Porosity was shown to have a more significant impact on elongation at fracture compared to the UTS and the YS, even at lower levels (< 1%) [62,38].

3.5.4. Fracture analysis

Analysis of the fracture surfaces for the strut and bulk sample has been performed in the search for differences that can affect the mechanical properties. Overall, in analyzing the fracture surfaces of strut and bulk samples, it can be noticed that the central portion is relatively flat, while toward the edges, shear lips at 45° compared to the loading direction are observed in Fig. 15. This behaviour is in agreement with previous studies [63,36]. High-magnification micrographs presented in Fig. 15 highlight the presence of deep dimples of similar sizes across all the analyzed conditions, regardless of the size and the orientation of the samples, which are frequently associated with the presence of ductile fracture [57,64]. The similarity of the dimple size stems from their fine $\alpha + \beta$ lamellar microstructure formed during the HT of the samples at 800 °C for 4 h. This microstructure promotes microvoid formation at the $\alpha \setminus \beta$ interfaces due to the strain and strength differences between the phases. [57,64].

The analysis of the fracture surface also supports the computational analysis presented in Section 3.5.1 on the load-bearing area. In the fracture images of Fig. 15, the surface corresponding to fractured material has been highlighted in red. Although the area is not directly correlated with the load-bearing area (as it depends on the amount of necking happening locally at the fracture surface before the fracture), some qualitative estimations can be made. It can be observed a larger ineffective area present in the HSS strut sample due to the high roughness compared to the one observed for LSS, where an outside layer of partially melted powder particles can be observed. These results are in agreement with the effective load bearing areas calculated in Section 3.5.1.

The high-magnification images for the HSS 90° strut specimen highlight that besides not being involved in the fracture area of the sample, the roughness forms notch-like features that promote stress concentration, as highlighted in Fig. 11, suggesting that the crack potentially initiates at the as-built surface, reducing the ductility of the sample [65,57]. This is in agreement with the tensile test strain-at-failure results of the struts, where for the 90° HSS strut, the average strain-at-failure

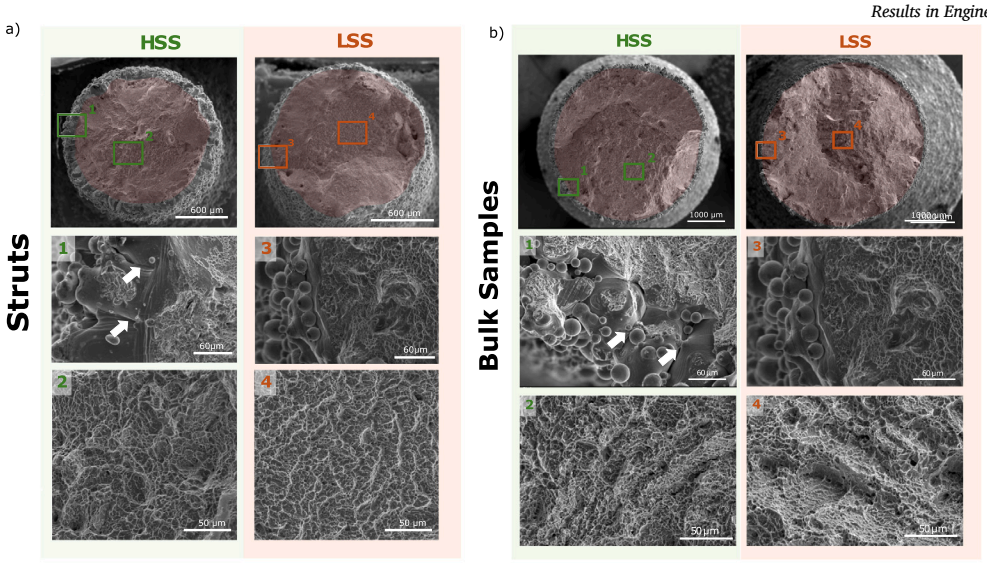

Fig. 15. Fracture surface of the HSS and LSS 90° strut and bulk specimens. In red, the load-bearing areas affected by the fracture are highlighted. High-magnification details show the difference in surface roughness and fracture details between the LSS and HSS samples.

measures 8.8 ± 0.5% versus 10.6 ± 1.0% measured for the LSS 90° strut. Similar features are observed also when analyzing the fracture surface of 90° of bulk samples, where HSS samples show high roughness with notch-like features, in contrast to the lower surface roughness in LSS samples. However, the layer affected by this phenomenon occupies a significantly smaller portion of the sample cross-section, resulting in a reduced impact on mechanical properties.

3.6. On the implications for the design of lattice structures

The implications of the results of this study on the design of lattice structures are several: the combined effects of the unloaded surface and the stress concentrations notches reduce the actual load-bearing area as the surface roughness acts like a series of closely spaced notches disrupting the stress flow. Roach et al. [50], in their study on LPBF 316L stainless steel flat miniaturized samples, observed similar findings. It is, therefore, reasonable to assume that a higher surface-to-volume ratio (i.e., thinner samples) further increases this effect as the proportion of unloaded area increases, enhancing the size effect. These findings underline the importance of the introduction of the concept of "inefficient mass" or "inefficient area" previously discussed by Suard et al. [54]. They highlight that due to the roughness effects on stress flow, not all mass contributes to bearing the stress, which indicates that a sample with lower mass could achieve the same mechanical performance. This concept is particularly relevant in lattice structures where thousands of struts form the structure, thus considerably affecting the mechanical properties and total inefficient mass of the structure.

It is clear that the estimation of the "inefficient area" and the tune of processing parameters to reduce it to the minimum can effectively enhance the reliability of additively manufactured parts. In any case, the roughness of AM printed parts remains an inherent challenge. Although it can be minimised through post-processing operations, it can not be fully eliminated. Several works have explored various approaches to reduce the roughness, including methods such as sand-blasting [66–68] and chemical etching [69–71]. However, while achieving consistent sandblasting of the internal cells in lattice structures remains challenging due to limited accessibility, chemical etching presents problems of localised and uneven material removal in strut-based structures modifying the geometry heterogeneously. This affect the dimensional accuracy and introduces an additional design variable, potentially compromising the repeatability of the mechanical properties across identical designs. For this reason, it is crucial to include the concept of efficient area at the design stage. In fact, using the full sample area in mechanical

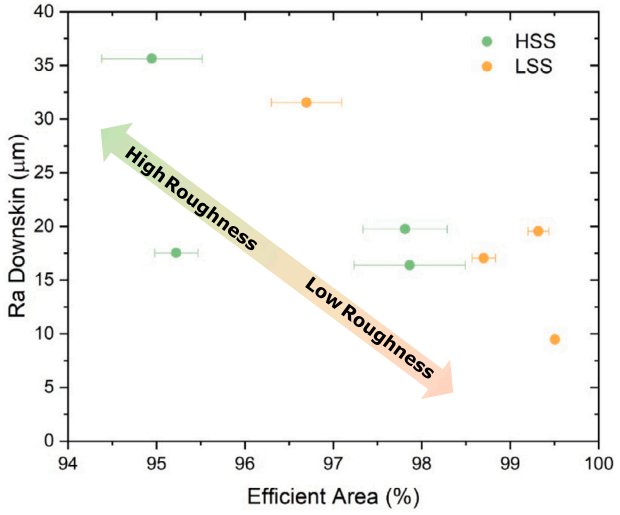

Fig. 16. Correlation between the efficient area calculated via FEM and the longitudinal downskin roughness of HSS and LSS struts.

simulations, without correcting for the inefficient portion caused by surface roughness and defects, might leads to an underestimation of local stresses and thus inaccurate mechanical predictions, for instance in terms of fatigue or crack initiation. Therefore, estimating this effective area properly at the design stage is critical. In this work, CT results combined with FEM simulations were used to calculate the effective area. However, this might not be possible for the wide range of strut sizes, inclinations, and processing conditions that might be considered at the design stage. For this reason, a possible estimation of the load-bearing area can be extracted from the longitudinal downskin roughness, as this is the main underlying cause for the inefficient area. To support this hypothesis, the correlation between the longitudinal roughness and the load-bearing area is presented in Fig. 16. As can be observed, there is a correlation, as increased roughness produces more protrusions and inclusion features at the surfaces, which leads to regions that do not carry load.

4. Conclusions

Despite starting from the same powder material, different regions of a LPBF component can be subjected to different thermal histories

and, therefore, present different microstructures and intrinsic mechanical properties that need to be considered. This set a challenge in the design of a component as the variations of the material and mechanical properties need to be understood. This study analyzes the influence of size, processing conditions, and orientation on LPBF Ti-6Al-4V mechanical performance. This work objective is two-fold: to analyze and compare the difference in mechanical properties and microstructure between large-size bulk samples and small-size elemental struts and to highlight the critical need for an accurate measuring method to characterize and assess the strut mechanical and material properties to ensure a reliable design. Based on the results, the following conclusions can be drawn:

1. **Effect of sample size:** Bulk specimens' yield strength (YS) and ultimate tensile strength (UTS) were inferior to smaller Ti-6Al-4V strut samples for LSS processing conditions. Increased strength in strut samples is correlated with a finer α-lath microstructure resulting from increased cooling rates during processing. Ductility was shown to be comparable in strut and bulk specimens, suggesting that the size effect starts to become more pronounced at smaller strut sizes than the ones considered in this study.
2. **Effect of Processing Parameters:** Higher scan speed (HSS) samples exhibited higher surface roughness that induced stress-concentration and increased the inefficient area, showing relatively lower mechanical properties compared to the samples printed with lower scan speed (LSS). LSS samples presented a more uniform distribution of stresses and superior load-carrying capacity, thus substantiating superior mechanical performance. The processing parameters effect was more pronounced on smaller samples due to their greater surface area-to-volume ratio.
3. **Effect of Printing Orientation:** Porosity, surface roughness, and mechanical characteristics were significantly influenced by build orientation. Struts printed at high inclinations (more horizontal) created higher surface roughness through excessive melting (dross formation), resulting in lower ductility. Optimal YS was found at mid-inclination angles (≈35°), where porosity was kept to a minimum while roughness was still acceptable.
4. **Load-Bearing Area Considerations:** A higher percentage of the outer material in high-roughness samples was not carrying any load compared to LSS samples. This underlines the importance of measuring the "effective" cross-section area rather than nominal dimensions to calculate the material mechanical properties. Finite element analysis (FEA) confirmed that high-roughness surface roughness induced stress concentrations, reducing overall mechanical performance.
5. **Implications for lattice structures:** These findings highlight the concept of "inefficient mass," where a portion of the printed sample does not effectively contribute to mechanical performance due to surface roughness and the resulting stress concentrations. In lattice structures, optimizing designs to account for the effective load-carrying area can lead to improved strength-to-weight ratios and improved use of material. The correlation between surface roughness and inefficient area might be used as an estimation at the design stage for more accurate results of the mechanical properties of cellular metamaterials.

CRediT authorship contribution statement

M. Casata: Writing – review & editing, Writing – original draft, Methodology, Investigation, Data curation, Conceptualization. **S. Perosanz:** Writing – review & editing, Methodology. **Y.T. Tang:** Writing – review & editing, Methodology. **T. Wilkinson:** Writing – review & editing, Methodology. **R.C. Reed:** Writing – review & editing, Supervision, Methodology. **D. Barba:** Writing – review & editing, Supervision, Investigation, Conceptualization, Methodology.

Declaration of competing interest

The authors declare that they have no known competing financial interests or personal relationships that could have appeared to influence the work reported in this paper.

Acknowledgements

This project has received funding from the European Union's Horizon 2020 research and innovation programme under the Marie Skłodowska-Curie grant agreement No 956401.

Grant EQC2019-006491-P funded by MICIU/AEI/10.13039/501100011033 and by ERDF A way of making Europe.

Appendix A

A.1. Statistical values of the porosity analysis

The median, mean, and, in particular, the maximum pore size measured by CT performed on the strut specimens are shown in Table A.1.

A.2. Influence of the methodology used in measuring the surface roughness of the material

The deviation between the two methodologies (OM and CT) used to analyze the surface roughness of the struts is calculated according to Equation (2) and is used to compare the two methods:

$$R_a^{\mathrm{DEV}} = \frac{R_{aOM}^{\mathrm{CS}} - R_{aCT}^{\mathrm{CS}}}{R_{aCT}^{\mathrm{CS}}} \cdot 100 \tag{2}$$

The calculated deviations are presented in Fig. A.1.

A.3. Influence of the methodology used in measuring the geometrical deviations

In this analysis, we consider the calculations obtained from CT analysis as the ground truth data as it can accurately provide a full 3D representation of the geometry of the printed material.

The measurements taken using a digital micrometer showed the largest deviations compared to the CT values, with greater deviation observed in the HSS parameter set and at higher strut inclination. The 2D OM longitudinal approach resulted in an overestimation of the area by an average of 9.9% for HSS and 5.8% for LSS, compared to CT. The measurement method with the smallest deviation from the CT data is the 2D cross-sectional approach, which underestimates the load-bearing area by no more than 6.5% regardless of the strut set and orientation. However, the deviation is notably smaller for the LSS set, aligning with the results obtained with the other characterization methods.

The reasons for the significant difference between the four methods are schematically explained in Fig. A.2. The measurements performed using the flat micrometer (Fig. A.2a) and the 2D OM longitudinal approach (Fig. A.2b) show that both methods approximate the area calculation based on a circle and an ellipse, respectively. In particular, the

Table A.1
Values of arithmetic mean, median, and maximum of the equivalent pore diameter for both struts set (HSS and LSS) at each strut orientation.

	Orientation (°)	Optical			CT		
		max (μm)	mean (μm)	median (μm)	max (μm)	mean (μm)	median (μm)
HSS	90	49.6	15.3	11.6	91.5	24.9	20.4
	54	73.2	17.7	11.0	91.5	24.6	20.1
	35	51.4	14.8	10.5	68.3	20.0	16.2
	20	39.0	12.4	9.8	98.7	17.7	15.0
LSS	90	47.4	12.5	10.2	83.1	24.4	19.1
	54	65.1	20.9	15.2	91.6	29.9	28.3
	35	45.4	13.7	8.8	69.2	18.2	13.9
	20	29.8	8.2	12.3	35.6	12.8	12.6

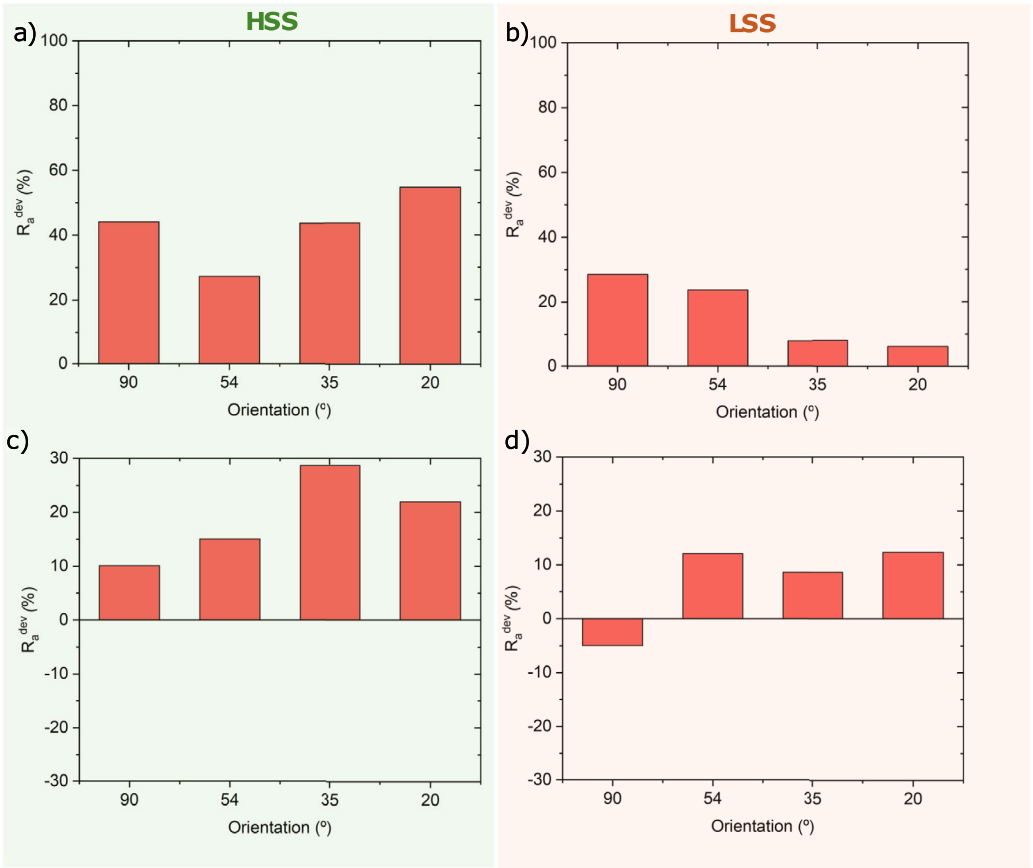

Fig. A.1. The deviation of 2D OM imaging compared against CT in CS a), b) and downskin roughness c, d for HSS and LSS struts.

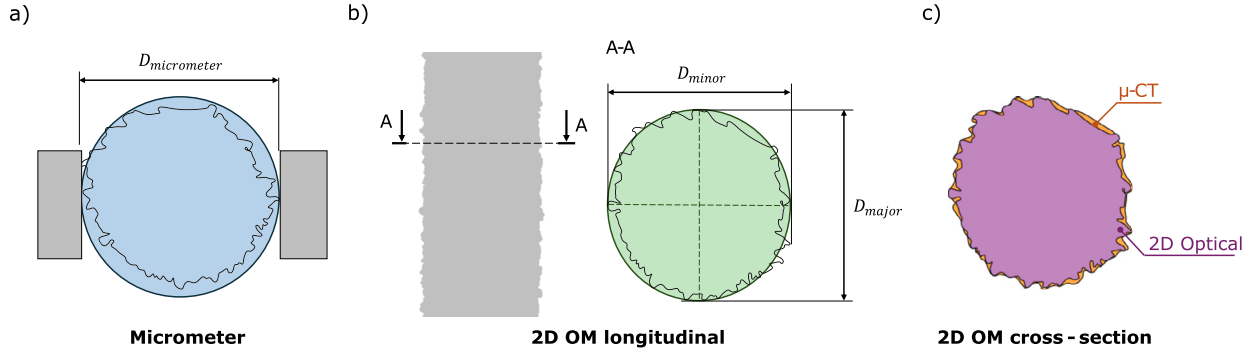

Fig. A.2. The approximation induced using the a) digital micrometer, b) the 2D OM longitudinal approach, and c) the 2D OM cross-sectional approach.

Table A.2
The deviation from the CT-measured area of the strut using the 2D OM longitudinal approach and its R_q adjusted version.

	Orientation (°)	Area Long. OM (mm^2)	Area CT (mm^2)	Area Long. OM Corrected (mm^2)	Deviation Long. OM/CT (%)	Deviation Long. OM Corrected/CT (%)
HSS	90	2.283	2.080	2.158	9.7	5.0
	54	2.380	2.152	2.233	10.6	4.6
	35	2.260	2.106	2.127	7.3	2.2
	20	2.280	2.038	2.094	11.9	4.6
LSS	90	1.993	1.863	1.893	7.0	3.8
	54	2.021	1.927	1.937	4.9	0.5
	35	1.915	1.866	1.806	2.6	-1.9
	20	1.940	1.784	1.829	8.8	2.9

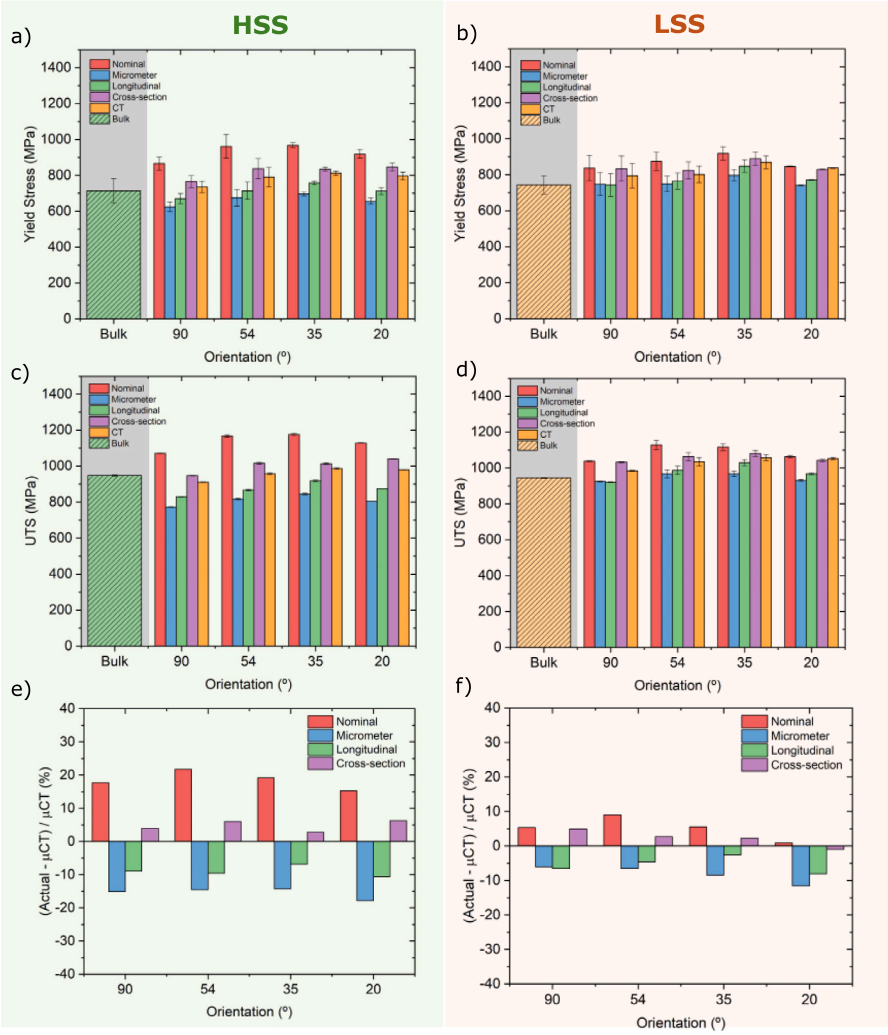

Fig. A.3. The mechanical properties, namely the YS and UTS and the deviation of the measurements methods from the CT of the HSS a), c), e) and LSS set b), d), f).

flat-end micrometer considers the Feret diameter [15], which results in a significant overestimation of the actual area of the sample. Furthermore, the high roughness of the strut increases the overestimation as the outer diameter is considered for the measurement, which explains the increasing deviation observed for HSS and higher strut inclination. Similarly, when evaluating the ellipse area using the 2D OM longitudinal approach, the Feret diameters of the 2D projections of the strut are considered as the minor and major axis of the ellipse, leading to an overestimation, (even though more accurate than the micrometer) of the true cross-sectional area. However, since the entirety of the gauge length is considered (similarly to CT), this method effectively takes into account and averages eventual deviations in the cross-sectional areas obtained along the gauge length (Fig. A.2b) providing a non-destructive method to measure the area.

To reduce the deviation measured with the 2D OM longitudinal approach and provide more accurate results, a correction based on the approach of Demenghi et al. [72] is proposed. The root mean square roughness (R_q) (Eq. (3)) is subtracted from both the major and minor axis of the ellipse to obtain a more accurate estimation of the cross-sectional area.

$$R_q = \sqrt{\frac{1}{n}\sum_{i=1}^{n} y_i^2} \tag{3}$$

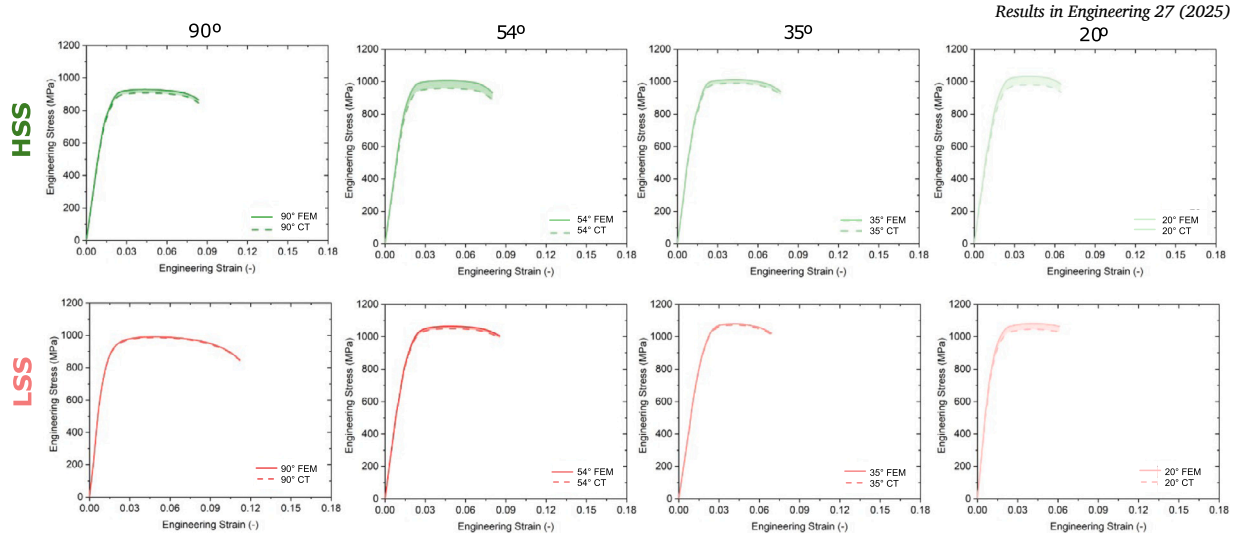

Fig. A.4. Representative stress-strain curves obtained for HSS and LSS struts using A_{ct} and A_{lb} are reported.

R_q is preferred over R_a since it represents the standard deviation of the distribution of the peaks and valleys, providing a better understanding of surface variability [73]. Table A.2 reports the deviation between the 2D OM longitudinal approach and the CT on the load-bearing area measurement obtained after applying this correction; the average deviation was reduced from 9.9% to 4.1% for HSS and from 5.8% to 2.3% for LSS. This correction is therefore considered a reliable approximation for estimating the load-bearing area using a non-destructive optical method, leading to results comparable to CT analysis.

Lastly, as discussed in Section 3.3, the discrepancy between CT and 2D cross-sectional approach is attributed to the resolution limitations of the CT analysis and the limited number of cross-sections evaluated with 2D OM. Fig. A.2c shows that the optical cross-section images have sharper and more defined edges compared to the CT images, which are constrained by the 4.9 μm voxel size resolution. This limitation results in a rough estimate of the surface roughness that ultimately leads to a slight overestimation of the load-bearing area when measured using CT. However, the CT analysis is expected to be more representative as it considers the entire gauge length of the specimen, particularly when significant variations are present along the gauge length.

A.4. Influence of the methodology used to calculate the effective area on the assessment of the mechanical properties

The yield stress (YS) and ultimate tensile strength (UTS) shown in Fig. A.3, were calculated and compared based on the load-bearing areas discussed in Section A.2.

The variations in the load-bearing area calculations observed between the different measurement methods shown in Fig. 10 directly impact the mechanical properties. Specifically, Fig. 10e shows that the area measured with the micrometer results in underestimated mechanical properties. The deviation from the CT measured data shows an increase with the inclination reaching up to 17.8% in the case of YS and UTS in HSS strut manufactured at 20°. Similar trends are observed with the 2D OM approaches for HSS struts, with a deviation of 10.6% and 6.2% for the OM longitudinal and the OM cross-section methods, respectively, at the same strut orientation. The measurement deviation is more visible in samples with higher surface roughness due to the overestimation effect of the load-bearing area, as explained in Section 3.4. Interestingly, the 2D OM cross-section in the case of LSS struts shows a unique trend with a lower deviation at higher inclination, highlighting the importance of selecting the appropriate measurement method according to the specific case.

Finally, a comparison between the stress-strain curves of the struts obtained using A_{ct} and A_{lb} is shown in Fig. A.4. This comparison highlights the influence of surface roughness on the calculated mechanical properties. For LSS, which reports a R_a^{CS} lower than 15 μm across all conditions, except at 20°, the variation between the two curves is minimal, with noticeable deviation (≥ 2.5%) observed only at that inclination. On the contrary, in HSS struts, independently of the orientation, a consistent difference (≥ 2.5%) is observed across all orientations when using A_{lb}, which can be attributed to the higher surface roughness of the specimens. This, as highlighted in Fig. A.3, leads to an underestimation of the measured mechanical properties. On the contrary, in bulk samples, when the mechanical properties calculated using the load-bearing area extracted from 2D longitudinal OM are compared with those obtained using the approach proposed by Demenghi et al. [72] described in Table A.2, a difference of only 0.75% and 0.87% for LSS and HSS, respectively, is measured. This confirms that the influence of surface roughness is less significant when a larger cross-sectional area is considered.

Data availability

Data will be made available on request.

References

[1] K. Saha, S. Acharya, C. Nakamata, Heat transfer enhancement and thermal performance of lattice structures for internal cooling of airfoil trailing edges, J. Therm. Sci. Eng. Appl. 5 (2 2013), https://doi.org/10.1115/1.4007277.
[2] D. Barba, E. Alabort, R.C. Reed, Synthetic bone: design by additive manufacturing, Acta Biomater. 97 (2019) 637–656, https://doi.org/10.1016/j.actbio.2019.07.049.
[3] F.S. Bobbert, K. Lietaert, A.A. Eftekhari, B. Pouran, S.M. Ahmadi, H. Weinans, A.A. Zadpoor, Additively manufactured metallic porous biomaterials based on minimal surfaces: a unique combination of topological, mechanical, and mass transport properties, Acta Biomater. 53 (2017) 572–584, https://doi.org/10.1016/j.actbio.2017.02.024.
[4] T.C. Dzogbewu, Laser powder bed fusion of ti6al4v lattice structures and their applications, J. Met. Mater. Miner. 30 (2020) 68–78, https://doi.org/10.14456/jmmm.2020.53.
[5] J. Liu, J. Ye, D.S. Izquierdo, A. Vinel, N. Shamsaei, S. Shao, A review of machine learning techniques for process and performance optimization in laser beam powder bed fusion additive manufacturing, https://doi.org/10.1007/s10845-022-02012-0, 12 2023.
[6] T. DebRoy, H.L. Wei, J.S. Zuback, T. Mukherjee, J.W. Elmer, J.O. Milewski, A.M. Beese, A. Wilson-Heid, A. De, W. Zhang, Additive manufacturing of metallic components – process, structure and properties, https://doi.org/10.1016/j.pmatsci.2017.10.001, 3 2018.
[7] M. Benedetti, A. du Plessis, R.O. Ritchie, M. Dallago, N. Razavi, F. Berto, Architected cellular materials: a review on their mechanical properties towards fatigue-tolerant design and fabrication, https://doi.org/10.1016/j.mser.2021.100606, 4 2021.
[8] A. du Plessis, S.M.J. Razavi, M. Benedetti, S. Murchio, M. Leary, M. Watson, D. Bhate, F. Berto, Properties and applications of additively manufactured metallic cellular materials: a review, https://doi.org/10.1016/j.pmatsci.2021.100918, 4 2022.

[9] M. Schmitt, F. Gerstl, M. Boesele, M. Horn, G. Schlick, J. Schilp, G. Reinhart, Influence of part geometry and feature size on the resulting microstructure and mechanical properties of the case hardening steel 16mncr5 processed by laser powder bed fusion, in: Procedia CIRP, vol. 104, Elsevier B.V., 2021, pp. 726–731.

[10] C. López-García, E. García-López, H.R. Siller, J.A. Sandoval-Robles, C.A. Rodriguez, A dimensional assessment of small features and lattice structures manufactured by laser powder bed fusion, Prog. Addit. Manuf. 7 (2022) 751–763, https://doi.org/10.1007/s40964-022-00263-0.

[11] A. Riensche, B.D. Bevans, Z. Smoqi, R. Yavari, A. Krishnan, J. Gilligan, N. Piercy, K. Cole, P. Rao, Feedforward control of thermal history in laser powder bed fusion: toward physics-based optimization of processing parameters, Mater. Des. 224 (12 2022), https://doi.org/10.1016/j.matdes.2022.111351.

[12] G. Mohr, M.A. Chaudry, N. Scheuschner, S.B. González, M. Madia, K. Hilgenberg, Thermal history transfer from complex components to representative test specimens in laser powder bed fusion, Prog. Addit. Manuf. (1 2024), https://doi.org/10.1007/s40964-024-00689-8.

[13] D. Barba, C. Alabort, Y.T. Tang, M.J. Viscasillas, R.C. Reed, E. Alabort, On the size and orientation effect in additive manufactured ti-6al-4v, Mater. Des. 186 (1 2020), https://doi.org/10.1016/j.matdes.2019.108235.

[14] J.S. Zhang, Y.T. Tang, R. Jin, A. Lui, P.S. Grant, E. Alabort, A.C. Cocks, R.C. Reed, On the size-dependent fatigue behaviour of laser powder bed fusion ti-6al-4v, Addit. Manuf. 79 (1 2024), https://doi.org/10.1016/j.addma.2023.103922.

[15] U. Hossain, S. Ghouse, K. Nai, J.R. Jeffers, Mechanical and morphological properties of additively manufactured ss316l and ti6al4v micro-struts as a function of build angle, Addit. Manuf. 46 (2021) 102050, https://doi.org/10.1016/j.addma.2021.102050.

[16] M. Casata, S. Perosanz, C. Garrido, D. Barba, A holistic study of the effect of geometrical and processing conditions on the static mechanical performance of lpbf strut elements, Mater. Des. 247 (11 2024), https://doi.org/10.1016/j.matdes.2024.113387.

[17] S. Murchio, M. Dallago, F. Zanini, S. Carmignato, G. Zappini, F. Berto, D. Maniglio, M. Benedetti, Additively manufactured ti–6al–4v thin struts via laser powder bed fusion: effect of building orientation on geometrical accuracy and mechanical properties, J. Mech. Behav. Biomed. Mater. 119 (7 2021), https://doi.org/10.1016/j.jmbbm.2021.104495.

[18] J.P. Rouse, M. Simonelli, C.J. Hyde, On the use of small ring testing for the characterisation of elastic and yield material property variation in additively manufactured materials, Addit. Manuf. 36 (12 2020), https://doi.org/10.1016/j.addma.2020.101589.

[19] J. Dzugan, M. Seifi, R. Prochazka, M. Rund, P. Podany, P. Konopik, J.J. Lewandowski, Effects of thickness and orientation on the small scale fracture behaviour of additively manufactured ti-6al-4v, Mater. Charact. 143 (2018) 94–109, https://doi.org/10.1016/j.matchar.2018.04.003.

[20] D. June, J.R. Mayeur, P. Gradl, A. Wessman, K. Hazeli, Effects of size, geometry, and testing temperature on additively manufactured ti-6al-4v titanium alloy, Addit. Manuf. 80 (1 2024), https://doi.org/10.1016/j.addma.2024.103970.

[21] G. Demeneghi, B. Barnes, P. Gradl, D. Ellis, J.R. Mayeur, K. Hazeli, Directed energy deposition grcop-42 copper alloy: characterization and size effects, Mater. Des. 222 (10 2022), https://doi.org/10.1016/j.matdes.2022.111035.

[22] B.B. Babamiri, H. Askari, K. Hazeli, Deformation mechanisms and post-yielding behavior of additively manufactured lattice structures, Mater. Des. 188 (3 2020), https://doi.org/10.1016/j.matdes.2019.108443.

[23] A. Burr, T. Persenot, P.T. Doutre, J.Y. Buffiere, P. Lhuissier, G. Martin, R. Dendievel, A numerical framework to predict the fatigue life of lattice structures built by additive manufacturing, Int. J. Fatigue 139 (10 2020), https://doi.org/10.1016/j.ijfatigue.2020.105769.

[24] J.D. Arputharaj, S. Nafisi, R. Ghomashchi, Printability and geometric capability of l-pbf in manufacturing thin circular cross-sections, J. Manuf. Process. 129 (2024) 319–340, https://doi.org/10.1016/j.jmapro.2024.08.054.

[25] M. Dallago, S. Raghavendra, V. Luchin, G. Zappini, D. Pasini, M. Benedetti, Geometric assessment of lattice materials built via selective laser melting-review under responsibility of 1st international conference on materials, mimicking, manufacturing from and for bio application (biom&m), www.sciencedirect.comwww.materialstoday.com/proceedings2214-7853, 2019.

[26] Dragonfly 2022.2 [Computer software]. Comet Technologies Canada Inc., Montreal, Canada; software available at https://www.theobjects.com/dragonfly.

[27] S. Murchio, A.D. Plessis, V. Luchin, D. Maniglio, M. Benedetti, Influence of mean stress and building orientation on the fatigue properties of sub-unital thin-strut miniaturized ti6al4v specimens additively manufactured via laser-powder bed fusion, Int. J. Fatigue 180 (3 2024), https://doi.org/10.1016/j.ijfatigue.2023.108102.

[28] A. du Plessis, P. Sperling, A. Beerlink, L. Tshabalala, S. Hoosain, N. Mathe, S.G. le Roux, Standard method for microct-based additive manufacturing quality control 1: porosity analysis, MethodsX 5 (2018) 1102–1110, https://doi.org/10.1016/j.mex.2018.09.005.

[29] K. Solberg, E.W. Hovig, K. Sørby, F. Berto, Directional fatigue behaviour of maraging steel grade 300 produced by laser powder bed fusion, Int. J. Fatigue 149 (8 2021), https://doi.org/10.1016/j.ijfatigue.2021.106229.

[30] E. Iso, 4287–Geometrical Product Specifications (Gps)–Surface Texture: Profile Method–Terms, Definitions and Surface Texture Parameters, International Organization for Standardization, Geneva, Switzerland, 1997.

[31] Y. Huang, A.R. Wan, K. Schmidt, P. Sefont, S. Singamneni, Z.W. Chen, Effects of cell orientation on compressive behaviour of electron beam powder bed fusion ti6al4v lattice structures, in: Materials Today: Proceedings, 2023.

[32] L. Meng, H. Yang, H. Ji, S. Wang, D. Ren, Z. Zhang, X. Shao, J. Yang, Z. Zhang, Effect of build thickness on defects, microstructure and mechanical properties of laser-powder bed fusion ti6al4v alloy, Mater. Sci. Eng. A (2025) 147931, https://doi.org/10.1016/j.msea.2025.147931, https://linkinghub.elsevier.com/retrieve/pii/S0921509325001492.

[33] C.M. Cepeda-Jiménez, F. Potenza, E. Magalini, V. Luchin, A. Molinari, M.T. Pérez-Prado, Effect of energy density on the microstructure and texture evolution of ti-6al-4v manufactured by laser powder bed fusion, Mater. Charact. 163 (5 2020), https://doi.org/10.1016/j.matchar.2020.110238.

[34] D.L. Wenzler, K. Bergmeier, S. Baehr, J. Diller, M.F. Zaeh, A novel methodology for the thermographic cooling rate measurement during powder bed fusion of metals using a laser beam, Integr. Mater. Manuf. Innov. 12 (1) (2023) 41–51, https://doi.org/10.1007/s40192-023-00291-w.

[35] A. Cardeña, R. Sancho, F. Gálvez, S. Perosanz, D. Barba, Multiscale study of the dynamic behaviour of additively manufactured ti6al4v cellular metamaterials, Int. J. Impact Eng. 202 (2025) 105294, https://doi.org/10.1016/j.ijimpeng.2025.105294, https://www.sciencedirect.com/science/article/pii/S0734743X25000752.

[36] M. Simonelli, Y.Y. Tse, C. Tuck, Effect of the build orientation on the mechanical properties and fracture modes of slm ti-6al-4v, Mater. Sci. Eng. A 616 (2014) 1–11, https://doi.org/10.1016/j.msea.2014.07.086.

[37] R. Yavari, Z. Smoqi, A. Riensche, B. Bevans, H. Kobir, H. Mendoza, H. Song, K. Cole, P. Rao, Part-scale thermal simulation of laser powder bed fusion using graph theory: effect of thermal history on porosity, microstructure evolution, and recoater crash, Mater. Des. 204 (6 2021), https://doi.org/10.1016/j.matdes.2021.109685.

[38] W.H. Kan, M. Gao, X. Zhang, E. Liang, N.S.L. Chiu, C.V.S. Lim, A. Huang, The influence of porosity on ti-6al-4v parts fabricated by laser powder bed fusion in the pursuit of process efficiency, Int. J. Adv. Manuf. Technol. 119 (2022) 5417–5438, https://doi.org/10.1007/s00170-021-08374-8.

[39] Q. Luo, L. Yin, T.W. Simpson, A.M. Beese, Effect of processing parameters on pore structures, grain features, and mechanical properties in ti-6al-4v by laser powder bed fusion, Addit. Manuf. 56 (8 2022), https://doi.org/10.1016/j.addma.2022.102915.

[40] Z. Dong, Y. Liu, W. Li, J. Liang, Orientation dependency for microstructure, geometric accuracy and mechanical properties of selective laser melting alsi10mg lattices, J. Alloys Compd. 791 (2019) 490–500, https://doi.org/10.1016/j.jallcom.2019.03.344.

[41] C. Phutela, N.T. Aboulkhair, C.J. Tuck, I. Ashcroft, The effects of feature sizes in selectively laser melted ti-6al-4v parts on the validity of optimised process parameters, Materials 13 (2020) 117, https://doi.org/10.3390/ma13010117.

[42] X.Z. Zhang, H.P. Tang, M. Leary, T. Song, L. Jia, M. Qian, Toward manufacturing quality ti-6al-4v lattice struts by selective electron beam melting (sebm) for lattice design, JOM 70 (2018) 1870–1876, https://doi.org/10.1007/s11837-018-3030-x.

[43] R. Vrána, T. Koutecký, O. Červinek, T. Zikmund, L. Pantělejev, J. Kaiser, D. Koutný, Deviations of the slm produced lattice structures and their influence on mechanical properties, Materials 15 (5 2022), https://doi.org/10.3390/ma15093144.

[44] J.S. Zhang, Y. Deng, H. Liu, Y.T. Tang, A. Lui, P.S. Grant, E. Alabort, R.C. Reed, A.C. Cocks, Orientation matters: assessing the cyclic deformation behaviour of laser powder bed fusion ti-6al-4v, Mater. Des. 248 (2024) 113485, https://doi.org/10.1016/j.matdes.2024.113485, https://linkinghub.elsevier.com/retrieve/pii/S0264127524008608.

[45] J.S. Zhang, Y.T. Tang, Y. Deng, H. Liu, A. Lui, P.S. Grant, E. Alabort, R.C. Reed, A.C.F. Cocks, Orientation matters: assessing the cyclic deformation behaviour of laser powder bed fusion ti-6al-4v, https://ssrn.com/abstract=4568921.

[46] V. Sundar, S. Ganti, B. Turner, Porosity analysis via 3d serial sectioning for additively manufactured alloy samples, in: Materials Science and Technology Conference and Exhibition 2017, MS and T 2017, vol. 1, Association for Iron and Steel Technology, AISTECH, 2017, pp. 328–335.

[47] G. Kasperovich, J. Haubrich, J. Gussone, G. Requena, Correlation between porosity and processing parameters in tial6v4 produced by selective laser melting, Mater. Des. 105 (2016) 160–170, https://doi.org/10.1016/j.matdes.2016.05.070, https://www.sciencedirect.com/science/article/pii/S0264127516306761.

[48] N. Koju, J. Hermes, S.E. Saghaian, L. Yang, Laser powder bed fusion additively manufactured thin lightweight ti6al4v features: an experimental investigation on the influence of powder feedstock, geometry, and process parameters on property/quality, Int. J. Adv. Manuf. Technol. 130 (3) (2024) 1541–1561, https://doi.org/10.1007/s00170-023-12712-3.

[49] I. Aiza, C. Baldi, F.M. de la Vega, S. Sebastiani, N.E. Veronese, M. Yousefi, M.H. Mosallanejad, E. Maleki, M. Guagliano, L. Iuliano, A. Saboori, S. Bagherifard, Effects of build orientation and inclined features on physical, microstructural and mechanical properties of powder bed fusion additively manufactured metallic parts, Prog. Mater. Sci. 147 (2025) 101357, https://doi.org/10.1016/j.pmatsci.2024.101357, https://www.sciencedirect.com/science/article/pii/S0079642524001269.

[50] A.M. Roach, B.C. White, A. Garland, B.H. Jared, J.D. Carroll, B.L. Boyce, Size-dependent stochastic tensile properties in additively manufactured 316l stainless steel, Addit. Manuf. 32 (3 2020), https://doi.org/10.1016/j.addma.2020.101090.

[51] Y. Tian, H. Ren, J. He, X. Zha, K. Lin, M. Zhou, Y. Xiong, Surface roughness improvement of ti-6al-4v alloy overhang structures via process optimization for laser-powder bed fusion, J. Manuf. Process. 110 (2024) 434–446, https://doi.org/10.1016/j.jmapro.2024.01.008.

[52] A. Charles, A. Elkaseer, U. Paggi, L. Thijs, V. Hagenmeyer, S. Scholz, Down-facing surfaces in laser powder bed fusion of ti6al4v: effect of dross formation on di-

mensional accuracy and surface texture, Addit. Manuf. 46 (10 2021), https://doi.org/10.1016/j.addma.2021.102148.

[53] F.H. Kim, H. Yeung, E.J. Garboczi, Characterizing the effects of laser control in laser powder bed fusion on near-surface pore formation via combined analysis of in-situ melt pool monitoring and X-ray computed tomography, Addit. Manuf. 48 (12 2021), https://doi.org/10.1016/j.addma.2021.102372.

[54] M. Suard, G. Martin, P. Lhuissier, R. Dendievel, F. Vignat, J.J. Blandin, F. Villeneuve, Mechanical equivalent diameter of single struts for the stiffness prediction of lattice structures produced by electron beam melting, Addit. Manuf. 8 (2015) 124–131, https://doi.org/10.1016/j.addma.2015.10.002.

[55] B.N.J. Persson, Surface Roughness-induced stress concentration, Tribol. Lett. 71 (2023) 66.

[56] W.D. Pilkey, R.E. Peterson, Peterson's Stress Concentration Factors, Wiley, 1997.

[57] P. Tao, H. xue Li, B. ying Huang, Q. dong Hu, S. li Gong, Q. yan Xu, Tensile behavior of ti-6al-4v alloy fabricated by selective laser melting: effects of microstructures and as-built surface quality, China Foundry 15 (2018) 243–252, https://doi.org/10.1007/s41230-018-8064-8.

[58] L. Zhang, W. Harrison, M.A. Yar, S.G. Brown, N.P. Lavery, The development of miniature tensile specimens with non-standard aspect and slimness ratios for rapid alloy prototyping processes, J. Mater. Res. Technol. 15 (2021) 1830–1843, https://doi.org/10.1016/j.jmrt.2021.09.029.

[59] B. Yang, W.Q. Sun, W.C. Jiang, M.L. Wang, M.C. Li, J.K. Chen, Comparative study of the tensile properties of a 1.25cr-0.5mo steel characterized by the miniature specimen and the standard specimen, Int. J. Press. Vessels Piping 177 (11 2019), https://doi.org/10.1016/j.ijpvp.2019.103990.

[60] S. Sneddon, Y. Xu, M. Dixon, D. Rugg, P. Li, D.M. Mulvihill, Sensitivity of material failure to surface roughness: a study on titanium alloys ti64 and ti407, Mater. Des. 200 (2 2021), https://doi.org/10.1016/j.matdes.2020.109438.

[61] J. Liu, J. Liu, Y. Li, R. Zhang, Z. Zeng, Y. Zhu, K. Zhang, A. Huang, Effects of post heat treatments on microstructures and mechanical properties of selective laser melted ti6al4v alloy, Metals 11 (10 2021), https://doi.org/10.3390/met11101593.

[62] T. Voisin, N.P. Calta, S.A. Khairallah, J.B. Forien, L. Balogh, R.W. Cunningham, A.D. Rollett, Y.M. Wang, Defects-dictated tensile properties of selective laser melted ti-6al-4v, Mater. Des. 158 (2018) 113–126, https://doi.org/10.1016/j.matdes.2018.08.004.

[63] N. Wawrzyniak, P. Wanjara, M. Brochu, M. Brochu, Measuring the tensile properties of ti6al4v fabricated by laser powder bed fusion: influence of specimen dimensions, Theor. Appl. Fract. Mech. 131 (6 2024), https://doi.org/10.1016/j.tafmec.2024.104419.

[64] F. Sikan, P. Wanjara, J. Gholipour, M. Brochu, Use of miniature tensile specimens for measuring mechanical properties in the steady-state and transient zones of ti–6al–4v wire-fed electron beam deposits, Mater. Sci. Eng. A 862 (1 2023), https://doi.org/10.1016/j.msea.2022.144487.

[65] A. Ghosh, A. Kumar, X. Wang, A.M. Kietzig, M. Brochu, Analysis of the effect of surface morphology on tensile behavior of lpbf ss316l microstruts, Mater. Sci. Eng. A 831 (1 2022), https://doi.org/10.1016/j.msea.2021.142226.

[66] X. Lu, W. Zhang, M. Chen, J. Wang, Effect of post-processing methods on the surface quality of ti6al4v fabricated by lpbf, Front. Mater. 10 (2023) 1126749, https://doi.org/10.3389/fmats.2023.1126749, https://www.frontiersin.org/articles/10.3389/fmats.2023.1126749/full.

[67] S. Baciu, S. Ilean, M. Gherman, V. Nedeff, L. Rusu, M. Andrei, Influence of process parameters for selective laser melting on the roughness of 3d printed surfaces in co-cr dental alloy powder, Materials 12 (23) (2019) 3932, https://doi.org/10.3390/ma12233932, https://www.mdpi.com/1996-1944/12/23/3932.

[68] A. Bernevig-Sava, D. Gheorghe, A. Pascu, F.I. Petrescu, Recent research progress in the abrasive machining and finishing of additive manufactured parts, Materials 17 (4) (2024) 719, https://doi.org/10.3390/ma17040719, https://www.mdpi.com/1996-1944/17/4/719.

[69] M.A.G. Bezuidenhout, A. Wilton, D.J. De Beer, I. Yadroitsava, I. Yadroitsev, Surface improvement of laser powder bed fusion processed ti6al4v by chemical etching, Addit. Manuf. Lett. 2 (2022) 100044, https://doi.org/10.1016/j.addlet.2022.100044, https://www.sciencedirect.com/science/article/pii/S2772369022000445.

[70] M.A.G. Bezuidenhout, I. Yadroitsava, I. Yadroitsev, Effect of chemical etching time on the fatigue behavior of ti-6al-4v manufactured by laser powder bed fusion, Fatigue Fract. Eng. Mater. Struct. 47 (1) (2024) 190–202, https://doi.org/10.1111/ffe.14392, https://onlinelibrary.wiley.com/doi/10.1111/ffe.14392.

[71] R.C. Goodhead, Chemical etching investigation on surface finish and fatigue performance of lpbf ti-6al-4v, Ph.D. thesis, Stellenbosch University, 2021, https://scholar.sun.ac.za/server/api/core/bitstreams/3e1be5bb-ef64-49ee-a5cb-1b2c1abe1c8e/content.

[72] G. Demeneghi, B. Barnes, P. Gradl, J.R. Mayeur, K. Hazeli, Size effects on microstructure and mechanical properties of additively manufactured copper–chromium–niobium alloy, Mater. Sci. Eng. A 820 (7 2021), https://doi.org/10.1016/j.msea.2021.141511.

[73] S.A.L. Grillini, 1 - Topography in bio-tribocorrosion, 2013.